Utrecht University

Master Thesis

Improving satellite-based estimations of UV index and dose

and first assessment of UV in a world-avoided

Author:
Evert Wiegant

Supervisors:
Dr. Jos van Geffen
Dr. Michiel van Weele
Dr. Ronald van der A
Dr. Sander Houweling

June 30, 2016

Utrecht University

Koninklijk Nederlands
Meteorologisch Instituut
Ministerie van Infrastructuur en Milieu

Abstract

Improving satellite-based estimations of UV index and dose and first assessment of UV in a world-avoided

by Evert Wiegant

The UV index (UVI) and dose (UVD) are quantities of UV irradiance weighted for its effect on organisms. Both quantities are widely used as informative tools or as proxies for UV irradiance, commonly used in e.g. skin cancer research. The UVI and UVD can be measured using groundbased spectrometers, or modelled using satellite observations of ozone. The Royal Netherlands Meteorological Institute has developed a UV model with a unique spatial and temporal coverage. This study describes the update of this model. Updates include changing the computation and data sets used, regarding: ground elevation, surface albedo, cloud cover and error estimation. The updated model is used to compute UVI and UVD from the long-term Multi-Sensor Reanalysis of ozone, and compared with ozone fields that would have been present if the 1987 Montreal Protocol had not been adopted. We find that the northern hemisphere ozone depletion event of 2011, which is greatly exaggerated in absence of the Montreal Protocol, has only little effect on UV irradiance. Comparing scenarios with and without Montreal Protocol, we find that by the year 2012 the implementation of the Montreal Protocol has prevented UV levels from shifting nearly 10 degrees poleward in summer, an increased global sunburn rate by 9.9%, while also preventing a 14.5% increase in (sun related) vitamin D production. For UVD thresholds relevant for vitamin D sufficiency, we found an order of magnitude estimation of the effect of the Montreal Protocol: Removing part of the ozone layer, which the Montreal Protocol prevented, has a similar effect on surface UV irradiance as removing all cloud cover throughout the year.

Acknowledgements

This thesis would not have been completed to my satisfaction as it is, without the help of my KNMI supervisors. In particular Jos, for never saying "nee" whenever I asked "Heb je even tijd?", and Michiel for challenging me and helping me when I got stuck in these challenges. The meetings with my UU supervisor Sander, although they were few, were very valuable to me. Thank you all.

I also thank Anja, Frits, Bart, Josine and Mendy for their financial and/or emotional support, and my friends and colleagues at the KNMI for making my stay so enjoyable.

Contents

List of Figures

List of Tables

Chapter 1

Introduction

A large part of the sun's light is invisible to humans. The wavelength of the light that reaches the earth's surface ranges from about 300 to 2500 nanometers. The wavelength of light visible to humans lies between 400nm (violet) and 700nm (red). Light outside this range, although not visible, is still important for humans and other life on earth. Infrared light, lying on one end of the visible spectrum (>700nm), can be felt as heat rays. Ultraviolet (UV) light, to the other end of the visible spectrum (<400nm), has various effects that cannot be felt directly. The skin produces vitamin D when exposed to UV radiation, but may also turn red (sunburn).

Information about the amount of UV light at the earth's surface should be communicated to the public, since the effect of UV radiation can be harmful. To provide univocal information, a standardized unit for solar UV light is needed: the UV index (UVI) (Vanicek et al. 2000, World Health Organization 2002). The UVI is a measure for the amount of solar radiation one would receive at solar noon (i.e. when the sun is highest in the sky) under a cloudless sky, spectrally weighted for its effect on white people's skin. Other than serving as an informative tool, the UVI is used as a proxy for UV irradiance for some skin cancer researches (e.g. Hatfield et al. 2009).

Informing a wide public on or doing research with the UVI requires sufficient data of the UVI. To be able to warn people a forecast of the UVI would be needed and doing research generally requires a consistent data set. In situ measurements of the UVI are conducted but are not world-wide or consistent. Satellites offer a way of measuring the atmosphere that is world-wide and consistent. The UVI itself is not measured by satellites, but other quantities - quantities important for the UVI - are measured. The total column ozone, for example, determines the majority of UV absorption. Ozone has been measured by satellites for over 4 decades (van der A et al. 2015) and is assimilated to produce forecasts a few days ahead (Eskes et al. 2003). This ozone data, among other data from satellites, allows us to calculate the UVI using a model.

Several institutes have been modelling the UVI for many years, as is conveniently expounded by Koepke et al. (1998). Many of these models use multiple scattering spectral schemes or fast spectral schemes. These models calculate single UVI values in the order of seconds or more and are thus incapable of providing global coverage at a relevant resolution within reasonable computation time. Empirical models, like our model, are much faster. However, empirical models are relatively simple, limiting their use to, for example, idealized atmospheric conditions (Madronich 2007) or specific locations (Burrows et al. 1994, Foyo-Moreno et al. 2007). Our model uses the computational speed of an empirical model, and is more widely applicable due to its fitting method.

In addition to computing the UVI, our model can also be used to compute the UV dose (UVD). The UVI is tailored for informing a wide public, but is not directly related to various health effects since it only represents a momentary value for each day. Some studies regarding skin cancer (e.g. Juzeniene et al. 2014) or vitamin D production (e.g. Holick et al. 2011) are related to the total amount of UV irradiance over a day: the UVD. The model computes the UVD by integrating over multiple UVI values at different solar zenith angles during a day, including a correction for the attenuation of UV light by clouds.

1.1 The UV model

An empirical model was developed by Allaart et al. (2004) using groundbased measurements of UV spectra in De Bilt and Paramaribo. This model was then applied to global assimilated ozone fields as derived from measurements by the satellite based instruments GOME (aboard ERS-2; 1995-2003) and SCIAMACHY (aboard ENVISAT; 2002-2012), as described by van Geffen et al. (2004) and van Weele et al. (2005). Since the end of the ENVISAT mission, ozone measurements from the GOME-2 instrument (aboard MetOp-A; 2007-present) are used. The ozone data assimilation system (Eskes et al. 2003) is driven by ECMWF global temperature, pressure and wind fields, allowing a forecast of the ozone field, and therewith of the UVI, for a few days ahead. The cloud cover information, currently available only over Europe, used to determine the UV dose comes from the SEVERI instrument aboard a series of Meteosat satellites. Forecast and archive UV data is released via $http://www.temis.nl/uvradiation/$.

A description of the emperical model to derive the UVI and its implementation to satellite measurements of ozone is given in Chapter 2.

1.2 This thesis

The technical aim of this project is to upgrade the UV model, to incorporate the latest available data records and advancing scientific knowledge in the determination of the UV data products. These improvements are discussed in Chapters 3 - 6.

The scientific aim is to quantify health benefits achieved by the 1987 Montreal Protocol regarding UV irradiance, which is discussed in Chapter 7. The UV model is applied to the observed multi-sensor reanalysis (MSR) ozone fields for the years 1978-2012 (van der A et al. 2015) and compared to the ozone field adjusted to represent the case in which the Montreal Protocol had not been adopted, as modelled by Chipperfield et al. (2015). We look for the largest change in UV as a result of change in ozone due to the Montreal Protocol by studying extrema and spatial and temporal averages in ozone and UV index and dose. We also consider implications for human health regarding skin cancer incidence and vitamin D deficiency by counting threshold exceedance of UVI and UVD.

Chapter 2

Background

2.1 UV index and dose

The UVI is defined as:

$$UVI = \frac{1}{25\text{mW/m}^2} \int S_{noon}(\lambda)\, E(\lambda)\; d\lambda \tag{2.1}$$

Here $S_{noon}(\lambda)$ is the solar irradiance at the earth's surface at solar noon and $E(\lambda)$ the action spectrum. The action spectrum weights the part of the spectrum relevant for an effect on the skin (e.g. erythema, or sunburn). Action spectra are discussed in more detail in the next section. Calculation of the UVI uses the irradiance at the earth's surface at solar noon under a cloudless sky. The result is a dimensionless quantity, with each unit of UVI representing 25mW/m^2.

The UV dose (UVD) is the second quantity that is calculated by the UV model. The UVD is the total amount of (spectrally weighted) UV irradiance over a day:

$$UVD = \int_{day} A_f(t) \left(\int S(\lambda, t)\, E(\lambda)\; d\lambda \right)\; dt \tag{2.2}$$

Here A_f is the attenuation factor by clouds. The UVD is like an integral over multiple UVI values without its constraints; irradiance at all times of the day are used, clouds are accounted for and the UVD is dimensional. The UVD is usually expressed in kJ/m^2.

2.2 Action spectrum

UV light is divided in three bands:

- UVA (315 - 400 nm)
- UVB (280 - 315 nm)
- UVC (100 - 280 nm)

Due to chemical properties of the atmosphere, the shortest wavelength UV light is absorbed more than UV light of longer wavelengths. As a result, the UVC band is entirely absorbed high in the atmosphere and does not reach the earth's surface. UVB is strongly absorbed and only a small fraction (3.8%)[1] will reach the surface. UVA is moderately absorbed and thus largely transmitted to the surface (53%)[1].

The effect of UV radiation on humans also differs per wavelength; short wave UV (UVB and UVC) has a larger impact than long wave UV (UVA). The weight of each wavelength is given by the so-called action spectrum. There are different action spectra for the different effects that UV radiation may have on life on earth (notably on human skin). Action spectra for the three effects the model can calculate are shown in figure 2.1a. These effects are erythema (or sunburn) (McKinlay & Diffey 1987), DNA damage (Bernhard & Seckmeyer 1997) and vitamin D synthesis (Bouillon et al. 2006). The UVI follows from multiplying the spectrum at the earth's surface with an action spectrum. This

[1] Percentages are based on standard spectra (ASTM Standard G173 - 03, Gueymard et al. 2002) using the hemispherical spectral irradiance as surface irradiance.

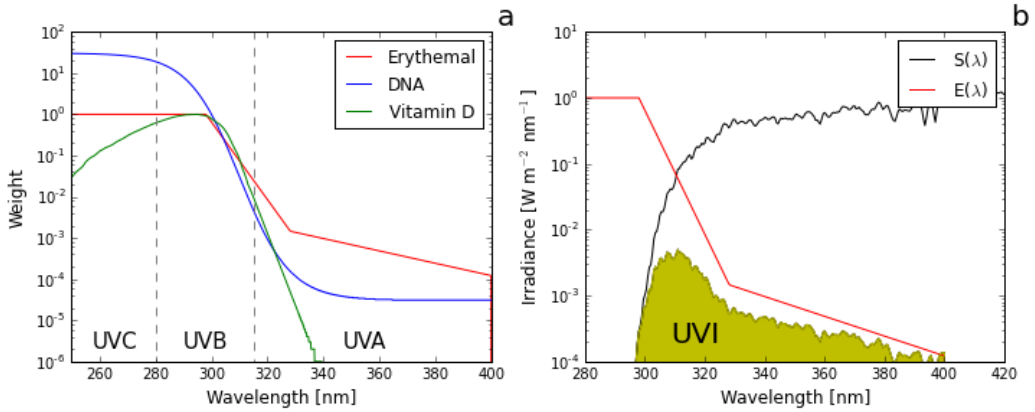

FIGURE 2.1: a) The action spectra for the different effects on human skin. b) A solar spectrum at the surface (black), the erythemal action spectrum (red) and the UVI (yellow area).

is shown in figure 2.1 for the standard hemispherical spectral irradiance (ASTM Standard G173-03) with the erythemal action spectrum, to get the erythemal UVI.

From figure 2.1a we can see that all effects of UV radation on human skin are weakest for long wave UV and strongest for shorter waves. The resulting erythemal UVI of figure 2.1b is composed for 45%[1] of UVA and for 55%[1] of UVB.

2.3 The model

Ozone is continuously being monitored by satellites orbiting the earth. These ozone measurements are assimilated in the TMDAM (Eskes et al. 2003) chemical transport model driven by ECMWF meteorology, providing consistent and continuous global ozone fields. Similar coverage of UV irradiance data cannot be provided by the scarce groundbased UV measurements. Modelling UV irradiance from ozone data will provide information on UV irradiance with the same coverage as the ozone data.

2.3.1 The model: Theory

The model calculates the UVI in two steps:

1. The contribution of the solar zenith angle (SZA) and total column ozone (TO) is computed.

2. Correction factors from other parameters (e.g. ground elevation and albedo) are applied.

The model calculates the UVD by integrating over multiple UVI (at different SZA's) with a time step of 5 minutes.

The relation between the UVI and parameters SZA and TO is deduced from several groundbased measurements during clear sky days at de Bilt and Paramaribo. This procedure is described in Allaart et al. (2004) and is not repeated here. The resulting function is as follows:

$$\frac{UVI}{UVA} = F \cdot X^G + \frac{H}{TO} + J \tag{2.3}$$

with

$$X = 1000 \cdot \frac{\mu_0}{TO}$$

and

$$\mu_0 = \cos(SZA)$$

	F	G	H	J
Erythema	2.0	1.62	280	1.4
Vitamin D	1.42	2.03	280	-0.51
DNA damage	0.54	2.46	150	-0.08

TABLE 2.1: Fitting parameters

UVA is the ozone-independent part of the UVI:

$$UVA = \left(\frac{D_0}{D}\right)^2 \cdot S \cdot \mu_x \cdot \exp\left(-\frac{\tau}{\mu_x}\right)$$

with

$$\mu_x = \mu_0 \cdot (1 - \epsilon) + \epsilon$$

Where SZA is the solar zenith angle, TO the total ozone column in Dobson units (DU), D the sun-earth distance, D_0 the average sun-earth distance, $\epsilon = 0.17$ an offset accounting for scattered light (fitted), $S = 1.24\text{W/m}^2$ the UVA at the top of the atmosphere (fitted), $\tau = 0.58$ the atmospheric extinction by molecular scattering and aerosol extinction (fitted) and F, G, H and J are fitting parameters characteristic for different action spectra. The values of these fitting parameters are shown in table 2.1.

With this fit function, the UVI depends on SZA and TO only. The next step is to apply correction factors for various quantities discussed below.

Ground elevation:
The UVI increases linearly by a set percentage per kilometer above sea level. A variety of percentages can be found in literature. At some stations in Tibet, an increase of UVI by 7-8%/km was found (Dahlback et al. 2007). The WHO (2002) states that UV radiation levels increase by 10-12%/km. We use a 5%/km increase of UVI as representative for the whole world (Badosa 2002):

$$f_h = 1 + 5 \cdot 10^{-5} * h \tag{2.4}$$

Where h is the ground elevation in meters and f_h the correction factor due to the ground elevation.

Albedo:
The albedo of the surface is the fraction of the light that is reflected back to the sky. The sky itself may then reflect light back to the surface. The intensity of the light that is reflected up and down is a fraction $\alpha_s\alpha_a$ (albedo of the surface and atmosphere respectively) of the original intensity. The total downward UV radiation is increased by a factor:

$$f_\alpha = 1 + \alpha_s\alpha_a + \alpha_s^2\alpha_a^2 + ... = \frac{1}{1 - \alpha_s\alpha_a}$$

We do not have real-time measurements of the albedo of the atmosphere. We therefore use $\alpha_a = 0.25$ as an approximation. The measurements for the fitting function of the UVI were performed in de Bilt and Paramaribo. The yearly average surface albedo is about 0.09 for both stations, which is corrected for. The final albedo factor becomes:

$$f_\alpha = \frac{1 - 0.25 \cdot 0.09}{1 - 0.25 \cdot \alpha_s} \tag{2.5}$$

Aerosols:
Aerosols also play a role in absorbing and scattering UV radiation which is not accounted for in the fitting procedure. Instead, the aerosol optical thickness (AOT) is assumed to be a constant 0.3 globally, introducing an error of about 5% (Badosa and van Weele 2002, Allaart et al. 2004).

Clouds:
Clouds are important only for the UVD; the UVI is defined as cloud-free (equation 2.2).

Data type	Source	Resolution (lon∗lat)	Time specification
Total column ozone	GOME-2 (Eskes et al. 2003)	1.5°∗1.0°	Near-real time
Ground elevation	GTOPO30 (Gesch et al. 1999)	30”	-
Albedo	TOMS/GOME (Boersma et al. 2004)	1.25°∗1.0°	Climatology
Cloud	MSG (Fernández et al. 2012)	$\gtrsim$3 km (disc)	Near-real time

TABLE 2.2: The data sets used in the UVI/UVD model. Cloud information for the UVD is only available for Europe.

The attenuation factor due to clouds is derived from groundbased measurements of the cloud cover fraction (CCF) (van Geffen et al. 2004, van Weele et al. 2005):

$$A_f = \begin{cases} 1 & CCF = 0 \\ 0.965081 - 0.255512 \cdot CCF & 0 < CCF < 1 \\ 0.5 & CCF = 1 \end{cases} \tag{2.6}$$

The overcast value (i.e. $CCF = 1$) is based on the average of multiple overcast measurements. A sky overcast with thin clouds allows more light to pass through than thick clouds, which cannot be recognized using satellite observations. Therefore, a wide range of attenuation factors are not distinguished by the satellite, as they all classify as overcast. The chosen attenuation factor is the average of all observed overcast attenuation factors (i.e. 0.5).

2.3.2 The model: Practice

The data required for the model is available in different formats. Details on the data sets used prior to the work of this thesis are found in table 2.2.

Ground elevation:
High-resolution data from a digital elevation model is resampled (averaged) to the grid on which the UV product is calculated (currently 0.5°). Other data sets are linearly interpolated to the centers of this grid.

Ozone:
As stated in table 2.2, ozone is provided real-time. Ozone maps are constructed with values that represent the local solar noon column value for every grid cell's center. This means that for a given day, a jump occurs along the date line (180° longitude); the adjacent grid cells differ by almost 24 hours. Since ozone values are not expected to vary much during a day, we use the same ozone data for calculation of the UVD.

Albedo:
Surface albedo data is not available near-real time. Therefore, monthly climatologies are used for a wavelength relevant for the UV products (currently 335nm). For each day, the current month determines which albedo map is used. For example, the computation for the 31st of March uses the albedo map of March and for the 1st of April the albedo map of April is used.

Clouds:
The cloud information that is used operationally is derived from the SEVIRI instrument on the METEOSAT second generation (MSG) satellites. These geostationary satellites measure every 15 minutes at a resolution of 3km at the equator, becoming gradually coarser towards the edge of the disc. The cloud information used is in the form of a cloud mask, giving information per pixel limited to ”cloudy”, ”cloud contaminated” and

"clear". Counting the cloud masks within a UV-grid cell ("cloudy" counts as 1, "cloud contaminated" as 0.5 and "clear" as 0) yields a cloud cover fraction (CCF). The CCF is then used to calculate the attenuation factor (equation 2.6). The cloud data currently only covers most of Europe.

The cloud information ultimately limits the resolution of the UV product. If clouds were ignored, grid cells can be as small as those of the ground elevation map, interpolating the other data to the same resolution. With clouds, the coarse resolution towards the edge of the disc becomes problematic. The cloud mask is a poor representation of actual cloud conditions, so a sufficient amount of MSG-pixels should be included in each UV-pixel for cloud information that is better representative for the whole grid cell.

Chapter 3

Elevation map

The elevation map used in the model prior to this thesis has a resolution of 0.5°. This map is derived from the GTOPO30 map (Gesch et al. 1999) by averaging the 30"∗30"-pixels that lie in each 0.5°∗0.5° grid cell. This elevation map will be replaced by a 0.25° resolution map derived from the GMTED2010 map (Danielson et al. 2011). The resolution change will be studied first; in section 3.1. The GTOPO30 map is averaged again to a 0.25° resolution map to which the GTOPO30-0.5° is compared. There may also be differences between the old GTOPO30 and the newer GMTED2010 maps. This is studied by comparing the GTOPO30-0.25° map to the GMTED2010-0.25° map.

The purpose of this change is to have each UV grid cell better represent the area it covers. A grid cell of 0.5°∗0.5° may cover multiple mountains and valleys. With a 5%/km height dependency, the UVD varies significantly in such areas which is not represented by the model. A 0.25°∗0.25° grid cell may still cover multiple mountains and valleys, but is an improvement nonetheless. The GMTED2010 map is accompanied by a data set giving the standard deviation of pixels from which the grid cell is averaged. This enables us to include the contribution from the variation in elevation to the error of the UV product. The UV product studied in this chapter is the clear sky UVD.

3.1 Resolution

The change in UVD solely due to changing resolution is studied in this section. The maps that are compared are the 0.5° and 0.25° versions of the GTOPO30 map.

3.1.1 Method

The effect on the UVD when changing the resolution is studied by subtracting the UVD on the fine grid from UVD on the coarse grid. This will yield four values for each cell on the coarse grid, from which the standard deviation (SD) is computed. The SD is expected to be high where gradients in the elevation (and the resulting UVD) are high. These SD therefore indicate how much the UVD changes at a certain location due to this change in resolution, and will be called the typical change value (TCV). This method is shown in figure 3.1 for some randomly generated "terrain".

Furthermore, we also look at the actual change (values indicated in color in figure 3.1) in elevation and UVD to see whether the expected 5%/km relation holds. This relation we call a, and will test a to see if it is indeed 5%/km. The UVD as a function of elevation h is given by (equation 2.4):

$$UVD(h) = UVD(0) \cdot (1 + a \cdot h)$$

The increase of UVD by a is an increase with respect to $UVD(0)$, which we do not know. We do know the UVD at a different altitude on the same pixel and thus the same $UVD(0)$ value:

$$\frac{UVD_1}{UVD_2} = \frac{UVD(h_1)}{UVD(h_2)} = \frac{1 + a \cdot h_1}{1 + a \cdot h_2}$$

Rearranging this equation, we find:

$$\frac{UVD_2 - UVD_1}{UVD_1} = a \cdot (h_2 - h_1 \cdot \frac{UVD_2}{UVD_1}) \tag{3.1}$$

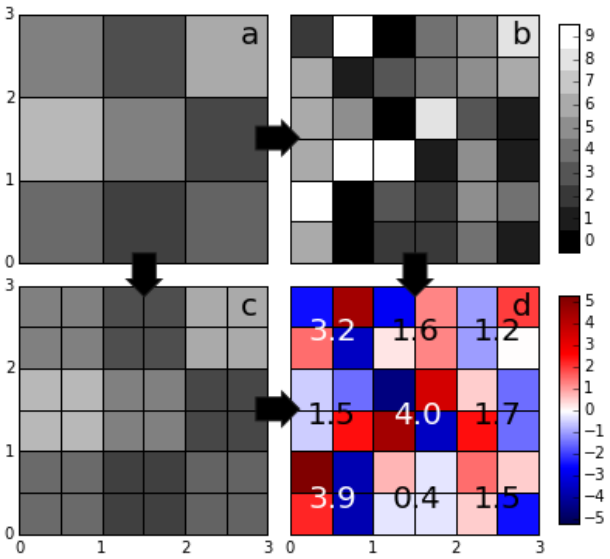

FIGURE 3.1: An example elevation map. a) A randomly generated surface elevation map. b) The corresponding higher resolution map. c) The map translated to a finer grid. d) Subtracting c from b yields four points per original grid cell (blue-red), of which the SD (or TCV) is calculated (shown numbers).

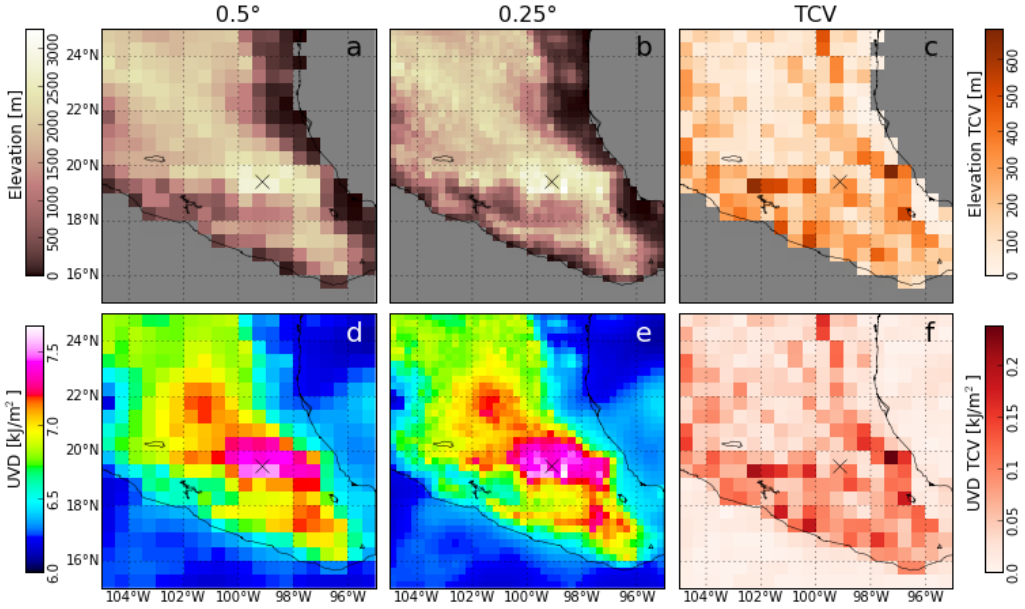

FIGURE 3.2: Change in elevation and the corresponding UVD change. a/b/c) Ground elevation on 0.5° and 0.25° resolution and its TCV respectively. d/e/f) UVD on 0.5° and 0.25° resolution and its TCV respectively. UVD data is from June 21st, 2012. The black 'X' marks the location of Mexico-city.

We find an equation that shows the relative change in UVD (a percentage) vs. (a corrected) height change (in meters) multiplied by the expected 5%/km relation. In practice, as we will see in section 3.2, this equation introduces unwanted rounding errors. To (largely) eliminate this, we multiply both sides by UVD_1:

$$UVD_2 - UVD_1 = a \cdot (h_2 \cdot UVD_1 - h_1 \cdot UVD_2) \tag{3.2}$$

3.1.2 Mexico-City

Mexico-City is located in the tropics in a mountainous region. The combination of high ground elevation and low SZA generally results in high UV values year-round. The presence of mountains means there may be large variations in elevation on the UV grids. This makes Mexico-City and surroundings an interesting region to study the effect of changing resolution.

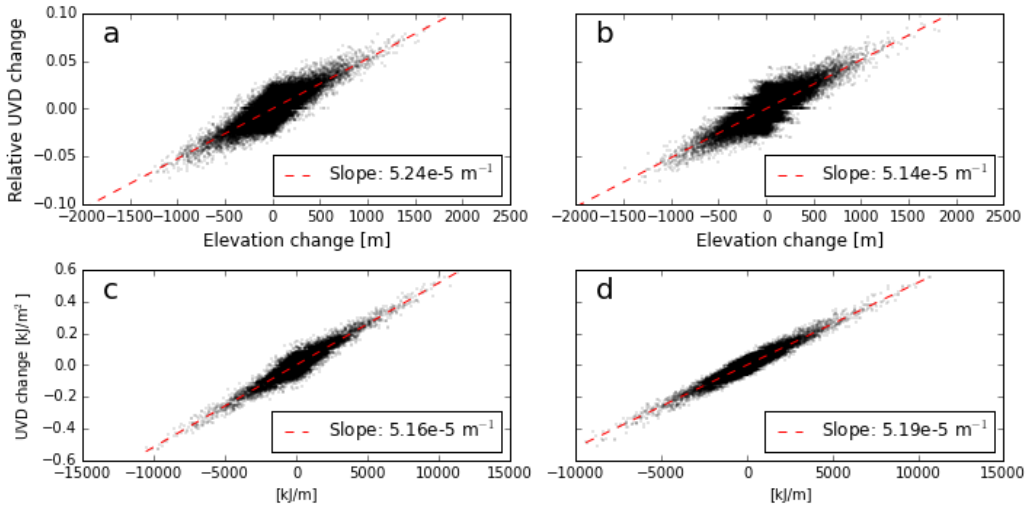

FIGURE 3.3: Changes in UVD and height resulting from changing elevation resolution, corresponding to equations 3.1 (a and b) and 3.2 (c and d). Dotted red lines show the least squares fit. a/c) March 21st, 2012. b/d) September 21st, 2012.

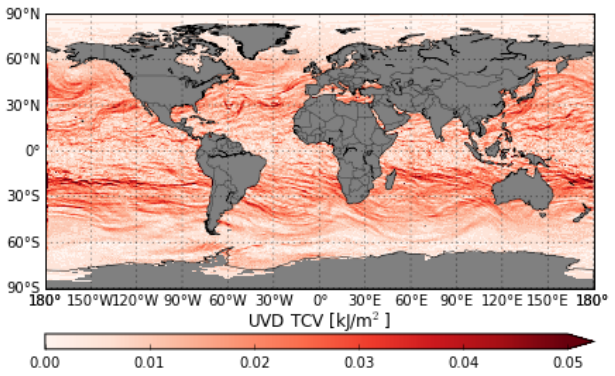

FIGURE 3.4: TCV of the UVD over water where the elevation is set to 0m on both 0.5° and 0.25° maps. The date is September 21st, 2012.

An area of 10°∗10° centered roughly on Mexico-City is shown in figure 3.2. Elevation and UVD are both shown on the 0.5° and 0.25°-grid, along with the resulting TCV. The TCV are large where the elevation gradient is large. Because of the simple linear relation between elevation and UVD (5%/km) we see a similar pattern in TCV of the UVD. Changing the model's resolution is therefore especially beneficial for people living near mountains (i.e. where elevation gradients are large).

For Mexico-City, the 0.5° grid cell that includes Mexico-City has an elevation value of 2747m. The 4 corresponding cells of the 0.25° grid have values 2979, 2857, 2878 and 2275m, with a TCV of 277m. The resulting change in the UVD ranges from 0.5 to 2%, or 0.03 to 0.15kJ/m^2.

3.1.3 The 5%/km relation

The model uses a 5%/km increase of UVD. If only the elevation changes, the UVD should change accordingly and a correlation of exactly 1 is expected. We will check this by including all land points that the model computes. To avoid division by zero (UVD may be zero, e.g. close to the poles) only points between latitudes 60°N and 60°S on an equinox day are included. The changes in UVD is plotted against changes related to height (according to equations 3.1 and 3.2) in figure 3.3.

The 5%/km relation is not exactly represented in the scatter plots of figure 3.3. The slope of the least squares fit comes close, but there is spread that cannot be explained from a change in elevation alone. This is because the change in elevation map has a twofold effect: One is already discussed (the 5%/km relation), the other is the slight displacement of the grid cell centers. The position of the grid cell center is used for calculating the

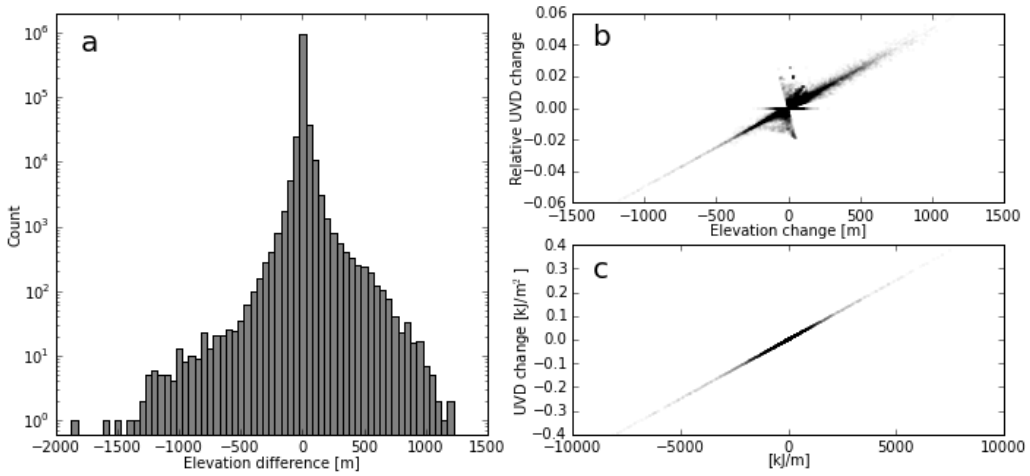

FIGURE 3.5: The difference between the GTOPO30 and GMTED2010 maps on 0.25° resolution, and the resulting effect on the UVD. a) The differences GMTED2010 minus GTOPO30 counted in bins of 50m width. b) Finding the 5%/km relation using equation 3.1, and c) using equation 3.2. Data are from September 21st, 2012.

solar zenith angles, which slightly changes as the latitude of the grid cell centers changes. The interpolated fields (i.e. ozone and albedo) also yield slightly different values when interpolated to a different location. We can see this is a real effect by looking at pixels over water (figure 3.4). Pixels over water have, by definition, an elevation of zero, so their elevation value does not change when changing resolution. The change over water appears to be largest where the gradients in the interpolated fields are largest (i.e. the ozone field) which is exactly as expected. To see whether this displacement effect is able to explain the spread in figures 3.3c and d, we can look at pixels over water. The spread from figures 3.3c and d are considered because they should not contain rounding errors.

To check whether the displacement effect explains the spread in figures 3.3c and d, the 5%/km dependency is subtracted from points over land, from which the SD is computed. The SD of the same day's points over water (including only points between 60°N and 60°S) is also computed. For the 21st of March, the SD over land is 0.020kJ/m^2, and 0.018kJ/m^2 over water. For September, the SD over land is 0.018kJ/m^2 and 0.016kJ/m^2 over water. We conclude that the spread in figures 3.3c and d is indeed due to the displacement of pixel centers. A slightly higher value over land is expected: Although ozone gradients should be similar over land and water, albedo gradients are expected to be higher over land.

3.2 Changing map

The change in resolution was studied by comparing the UVD computed with the GTOPO30-0.5° map to the UVD computed with the GTOPO30-0.25° map. In this section the change from GTOPO30-0.25° to GMTED2010-0.25° is studied.

The difference between maps is calculated by subtracting values of the GMTED2010- from the GTOPO30 map. Differences over 10m occur scattered across the world. Larger differences (over 100m) occur mostly around Antarctica and especially on Greenland, and rarely on the rest of the world. About 67% of grid cells remain exactly unchanged. The number of times each difference occurs is shown in a histogram in figure 3.5. Note that the counts (y-axis) are on a logarithmic scale. About 91% of points occur in the bin centered on 0 (i.e. between -25m and +25m difference).

Figures 3.5b and c show that the 5%/km relation is found ($= 4.9998... * 10^{-5}\text{m}^{-1}$ for figure c). The difference in both figures shows visually the effect of rounding errors. Points deviating from the 5%/km line have low UV values and usually lie close to the poles. Including only points between 60°N and 60°S excludes points lying furthest from the 5%/km line, looking similar to 3.5c.

The effect of this change is mostly small; changes over 100m occur rarely in the (inhabited) world. Such a change would lead to a change of UVD or UVI of 0.5% at most. This is unlikely to be significant for any weather information service or research based on UV levels.

Chapter 4

Albedo climatology

The albedo climatology used in the model prior to this thesis is a combination of Lamber-equivalent reflectivity (LER) data sets from the TOMS (Herman & Celarier 1997) and GOME (Koelemeijer et al. 2003) instruments at 335nm. Its method of construction is described by Boersma et al. (2004). The albedo map that is implemented in the model is the LER data set constructed from GOME-2 measurements (Tilstra et al. 2015) at 340nm. The UV product studied in this chapter is the clear sky UVD.

4.1 Changing maps

Changing to the GOME-2 LER data set is not an obvious improvement. The expected major improvements are due to the higher spectral resolution of the GOME-2 observations, which is expected to lead to smaller errors in the albedo. Unfortunately we cannot compare errors on the albedo climatology because the old TOMS/GOME data set does not include information on the error or accuracy. The major disadvantage of the new albedo data set is the time range from which the climatologies are constructed. The TOMS data set is constructed from measurements during 1978 to 1993 (16 years), so the combined TOMS/GOME data set has the same time range. The GOME-2 data set includes measurements from 2007 to 2013 (6 years).

A long measuring time is essential for the LER climatologies, or climatologies in general. Constructing a climatology from outlying conditions, e.g. multiple consecutive warm years, results in a biased climatology (e.g. not representative for colder years). Also, the albedo cannot be retrieved from cloudy pixels (the ground is not visible). The global average cloud cover is about 0.68 (Stubenrauch et al. 2013), meaning that there are only about 9 - 10 days per month with viable pixels. However, the GOME-2 data set is continuously being extended; the version to be used in the model includes data up to 2013 but is easily replaced in the future. The primary reason the GOME-2 data set is implemented is its higher spectral resolution. The albedo of both data sets for a particular month (March) is shown in figure 4.1.

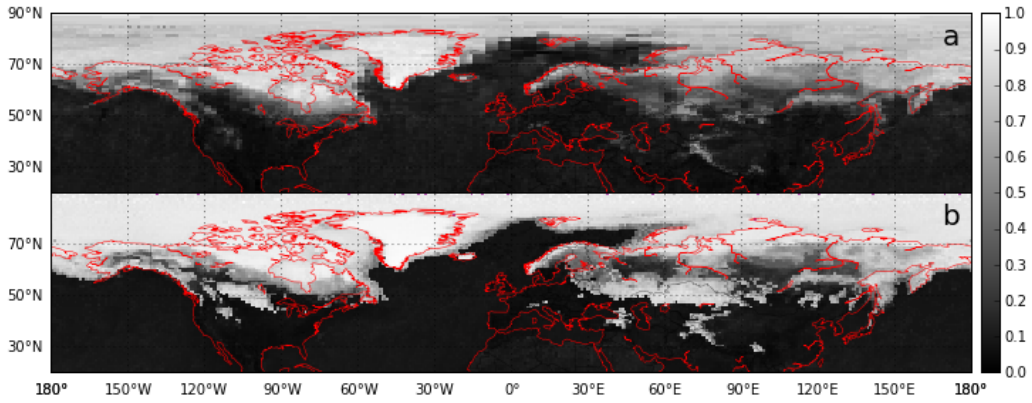

FIGURE 4.1: The LER climatology of the old and new data sets for March. Only the northern hemisphere (20°- 90°) is shown as this is where most differences occur. The data sets are a) TOMS/GOME (1.0°∗1.0°), b) GOME-2 (1.25°∗1.0°).

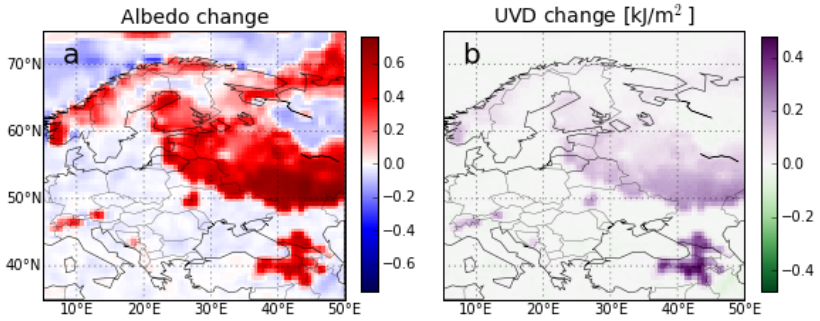

FIGURE 4.2: Subtracting the TOMS/GOME albedo map from the GOME-2 map on the 0.5°grid shows the difference in; a) albedo, b) UVD.

Although the TOMS/GOME and GOME-2 data sets have resolutions of 1.0°∗1.0°and 1.25°∗1.0° respectively, the data sets are compared on the 0.5°∗0.5° interpolated grid. The LER of GOME-2 is generally higher than that of TOMS/GOME. Including only pixels where a change occurs at all (absolute difference over 0.01), an increase of almost 0.1 is found. An average increase of 0.06 is found if all points are included. This is a large difference, but explaining this difference is out of the scope of this thesis as we are concerned with the resulting UV only. Depending on the albedo per pixel, an increase of 0.1 leads to an increase of about 3% in UVD (equation 2.5). Using data from March 15th, 2012, we indeed find the 3% average increase in UVD for pixels following the same criteria (including only albedo differences over 0.01) and excluding pixels on which $UVD = 0$ to avoid division by zero.

The 3% average increase seems substantial, but its relevance is limited. The average absolute increase in UVD is only about 0.02 kJ/m^2. A physical cause for difference in albedo between both maps (figure 4.1), and variation in albedo in general, is snow cover. Snow tends to be located where there is little sunlight and low UV levels as a result. Figures 4.2a and b show the difference in albedo and the corresponding difference in UVD on March 15th, 2012, for eastern Europe/western Asia. A clear gradient is visible towards lower latitudes. However, at lower latitudes, high albedo values become less abundant. Only in mountainous areas high values in albedo (and albedo change) are found. Correct information on UV irradiance - regarding the albedo factor - is therefore most important for inhabitants of mountainous regions at lower latitudes. UV levels tend to be high here due to smaller solar zenith angles and high ground elevation.

4.2 Wavelength

The albedo is wavelength dependent, which is seen from the color of the surface. Oceans have relatively high albedo in the short-wavelength part of the spectrum, resulting in a blue colour. Deserts generally reflect more in higher wavelengths and thus appear yellow/red. The fact that the sky appears blue is related to the high amount of scattering in short wavelengths. The satellite observes the earth's surface from sunlight that is reflected off the earth unscattered. Because scattering in the atmosphere occurs more for short wavelengths, the earth's surface (and the LER) is more difficult to measure at short wavelengths, resulting in larger uncertainties.

An additional minor change when changing from the TOMS/GOME to GOME-2 data set, is changing the wavelength for which the albedo is relevant. The wavelength at which the UVI peaks is near 310nm (figure 2.1), which is well below what is available as wavelength for the albedo from satellite measurements. Choosing the relevant wavelength is therefore a matter of picking the best of what is available. The GOME-2 LER is available for two wavelengths close to 310nm: at 335nm and 340nm. The mean difference between the wavelength's maps (map of 335 minus 340) is $7.0 * 10^{-3}$ whereas the difference in error is $1.7 * 10^{-3}$. These are very small differences, so either map should be fine. We choose the GOME-2 albedo map with the lowest error (i.e. the 340nm map) because this should

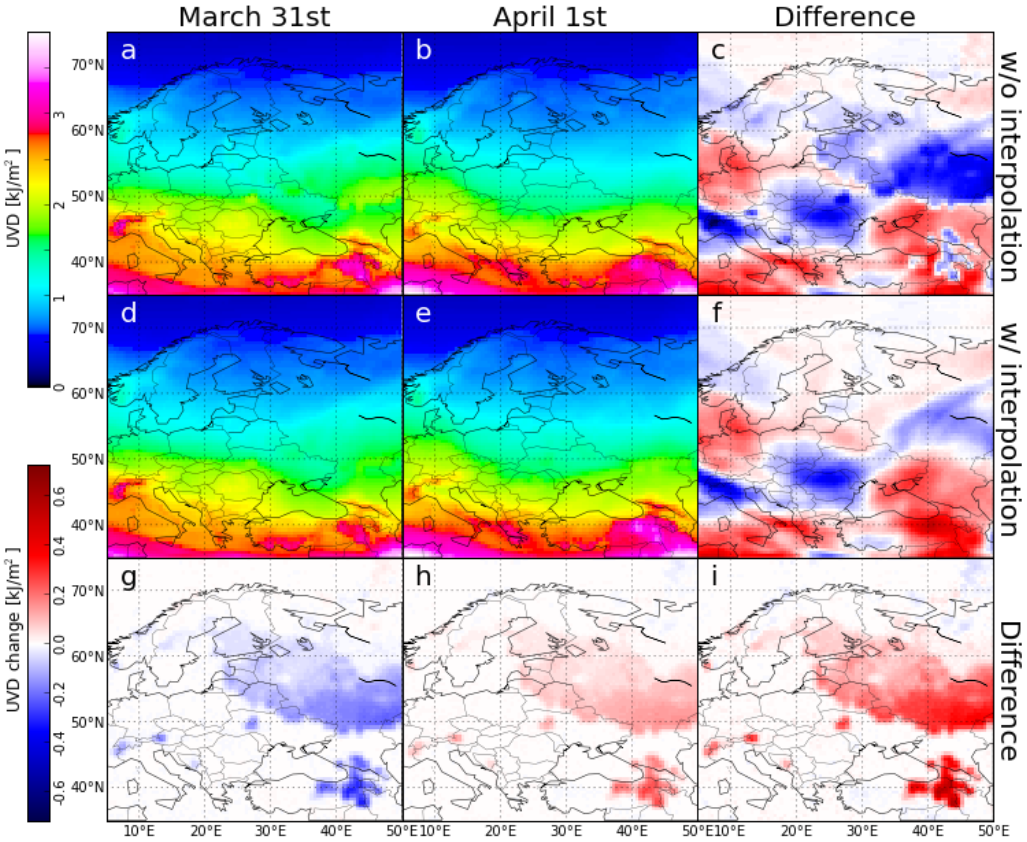

FIGURE 4.3: The UV dose change due to the addition of time-interpolating albedo maps of subsequent months. Going from a/d to b/e, the UVD has changed by the amount of c/f. The top 3 plots (a,b,c) show UVD on a map that is *not* interpolated in time. Plots (c,d,f) show UVD on an albedo map that *is* interpolated in time. The difference with minus without interpolation is shown in g/h for March 31st/April 1st. The difference in differences is shown in i ($= f - c = h - g$).

contain fewer pixels with high errors (outlier values). We think reducing the amount of outliers is more important than a better wavelength representation of the UVI.

4.3 Time interpolation

Prior to this thesis, all days in a month used the same albedo map. Large variations in albedo can occur from month to month due to snow fall/melt, especially at high latitudes. UV levels may therefore show a jump after the last day of a month, which is unrelated to any physical effects. We implement time interpolation between the month's climatologies to daily values to more realistically represent actual conditions on a certain day.

To compute the albedo map for a given day, linear interpolation is performed between the current month's map and the next- or previous month's map (next; if the date is after the 15th, previous if the date is before the 15th). The 15th of each month uses only the current month's map. The temporal resolution of the interpolation is limited to days; the UVD computed on one day uses the same albedo map for each time step.

The change in UVD due to the addition of time interpolation is shown in figure 4.3 for the 31st of March and 1st of April of 2012. The albedo map of March (figure 4.4a) contains some areas with high albedo values that are not present in the map of April (figure 4.4b), notably a large part of Russia and the Caucasus mountains. This causes the UVD to decrease strongly from March 31st to April 1st; by about 0.4kJ/m^2 over Russia and up to 0.2kJ/m^2 in the Caucasus mountains (figure 4.3c). With time interpolation the UVD decreases much less over Russia and increases in the Caucasus mountains (figure

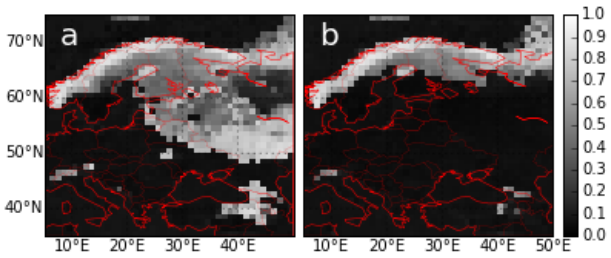

FIGURE 4.4: The GOME-2 LER maps of a) March and b) April, at 340nm wavelength.

4.3f). The difference in UVD between with and without interpolation when going from March 31st to April 1st (figure 4.3i) goes up to 0.6kJ/m^2 in the Caucausus mountains.

The conclusion of section 4.1 is again valid here. Areas towards low latitudes benefit most from a good albedo representation, particularly if the albedo tends to be variable (e.g. due to snowfall). Mountain ranges allow snowfall to occur at lower latitudes. Combined with the already high UV levels due to the elevation, variations in albedo cause relatively large variations in UV levels.

Chapter 5

Error estimation

With the usage of newer elevation and albedo data we have access to better error information on these quantities. In this chapter we present the error resulting from each quantity and the resulting total error in the UV product. The UV product studied in this chapter is the clear sky UVD.

5.1 Error calculation

The error on the UVI and UVD was, prior to this thesis, derived solely from the error in the ozone field. With the updates of the elevation map and surface albedo climatology, it is possible to comprise the UV error of the errors in ozone, elevation and albedo. The errors represent the standard deviation on each quantity. Since the quantities (ozone, elevation, albedo) are independent, we can add the errors in quadrature:

$$\sigma_{UV} = \sqrt{(\frac{\partial UV}{\partial O_3}\sigma_{O_3})^2 + (\frac{\partial UV}{\partial h}\sigma_h)^2 + (\frac{\partial UV}{\partial \alpha}\sigma_\alpha)^2} \tag{5.1}$$

where variables and subscripts UV, O_3, h and α indicate UVI or UVD, ozone, ground elevation and albedo respectively, σ's are errors on the respective quantities.

5.2 Resulting errors

The errors on the UVD related to ozone, elevation, albedo, and their combination are shown in figure 5.1 for March 21st, 2012. Numerical values of UV errors are listed in table 5.1 for both equinox days of 2012. Note that these are all errors in UVD (unit kJ/m^2), with each error resulting from a different quantity X, following:

$$\sigma_{UVD} = \frac{\partial UVD}{\partial X}\sigma_X \tag{5.2}$$

Figure 5.1b shows the error in UVD due to the error in ozone. Note that this was the total error in UVD prior to this thesis. Comparing the error due to ozone to the errors due to elevation and albedo, we find that the ozone error dominates over most parts of the world. Because the errors are added in quadrature (equation 5.1), the total error's pattern is very similar to that of the ozone error. Nevertheless, including the elevation error is relevant in specific places. Simply the act of standing on top of a mountain or in a valley within a grid cell gives rise to a range of possible values of UVDs that one could receive. The error is, apart from its statistical relevance, an important part of the information provided by the UV product.

From table 5.1 and figure 5.1 we can see how the contributions of different errors compare. The general pattern of the error is determined by the ozone error, which has a large mean but moderate maximum. The error due to ground elevation ('height' in table 5.1) error has a very small mean and is only relevant at specific locations. The maximum error due to the error in ground elevation is very large, signifying the relevance of the height error. The albedo error has a similar profile to that of the ozone error, with lower mean and comparable maximum. Therefore, the albedo error contributes only slightly to the total UVD error. Note that a spike has been excluded from table 5.1 that occurs near 65°S, 130°W. This spike contains values up to 1.49 kJ/m^2 which are not considered relevant for comparison.

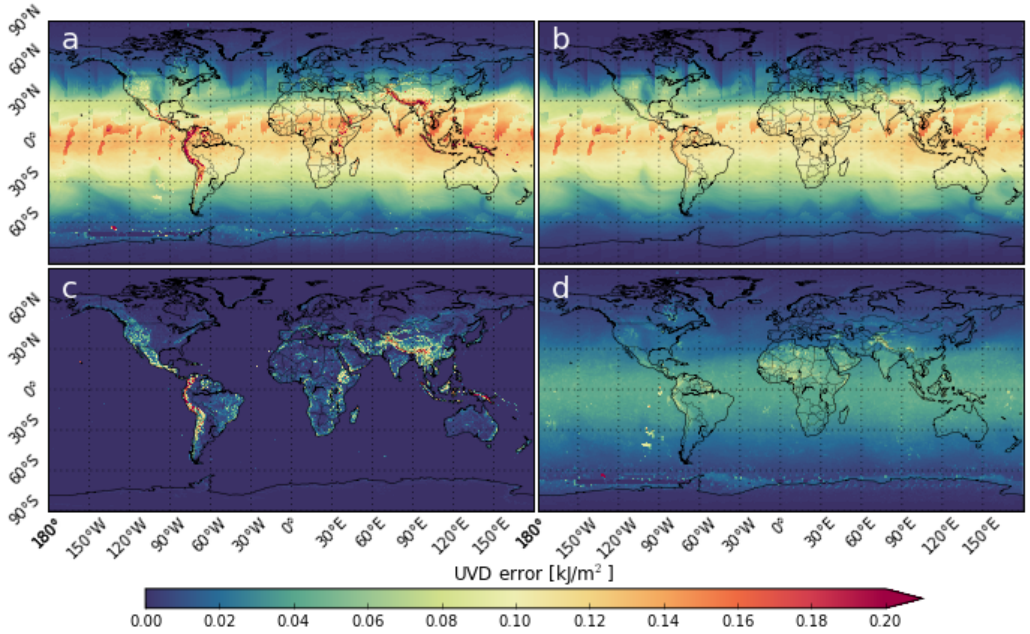

FIGURE 5.1: Errors in UVD of March 21st, 2012 due to errors in different quantities. a) The total error, resulting from adding the separate contributions in quadrature. Other errors are solely due to: b) ozone error, c) height error, d) albedo error.

Error	Mean [kJ/m^2]	Maximum [kJ/m^2]
Total	0.052	0.43
Ozone	0.047	0.19
Height	0.003	0.40
Albedo	0.020	0.24

March 21st, 2012

Error	Mean [kJ/m^2]	Maximum [kJ/m^2]
Total	0.054	0.43
Ozone	0.049	0.27
Height	0.004	0.37
Albedo	0.018	0.15

September 21st, 2012

TABLE 5.1: The mean and maximum of different parts of the UV dose error.

5.3 Discussion

It is important to note that the total error is not solely resulting from uncertainties of measurements. The elevation error is known to great detail and its error is no result of measurement uncertainties, but is the standard deviation of sub-0.25° pixels from which the 0.25° grid is comprised. The total error in UVD thus indicates the range of possible UVD values that one could measure anywhere in the grid cell. The UV error provides information on the reliability of the UV value, which is exactly what is achieved by including the elevation error.

Chapter 6

Revision of cloud attenuation

Simple cloud information has been available for the model in the form of a cloud mask from which a cloud cover fraction (CCF) is calculated. The CCF is translated to the cloud attenuation factor (CAF) by means of a fitted curve (equation 2.6). Information on the cloud mask is provided on the grid of the disc as viewed by the SEVIRI instrument aboard the geostationary MSG satellite located at (0°, 0°). The cloud data currently covers most of Europe: the same area used by the operational KNMI weather forecast system.

At present, more detailed cloud information is available in near-real time. This data is provided on the full disc retrieved from the MSG satellite. The cloud information is computed by the SICCS (Surface Insolation under Clear and Cloudy skies derived from SEVIRI imagery) (Greuell et al. 2013) algorithm and includes, among other properties, a cloud mask, cloud optical thickness (τ), cloud droplet effective radius (r_{eff}), total surface downwelling radiation (SDS) for the actual sky, and a SDS assuming clear sky conditions.

Recent developments have made it possible to calculate SDS for 6 wavelength bands separately. The UVD is determined by light of short wavelengths only. The SDS for bands of short wavelengths may therefore give a good representation of cloud effects in the UVD; better than the total (broad band) SDS would. However, the SDS data set for separate bands is small and not available in near real-time. The current MSG data is available from January 19th, 2004 to the day before the current date. The SDS for separate bands has been calculated for August 2014 only.

We thus have three data sets available; the old-style near-real time cloud mask, the newer near-real time data containing various cloud properties, and the very new limited time data of SDS per band (instead of broad band). In this chapter we look at how the newly available data can be applied to the model, with the result of improving the cloud effect on the UVD. The method of using the new data is described and a comparison to the previously used method is made.

The UV product studied in this chapter is the UVD. The UVI product is not affected by change in cloud computation as it is strictly computed for clear sky.

6.1 Problem: Representing the CAF

We seek a number that, multiplied with the clear sky UVD (UVD_{CS}), yields the cloudy sky UVD. This number is the CAF, which is defined as:

$$CAF \equiv \frac{UVD}{UVD_{CS}} \tag{6.1}$$

In reality, the CAF may be wavelength dependent. The CAF for a cloudy UVD-rate at time t is then given by:

$$\frac{UVD(t)}{UVD_{CS}(t)} = \frac{\int_{280}^{400} S(\lambda,t)\ E(\lambda)\ CAF(\lambda,t)\ d\lambda}{\int_{280}^{400} S(\lambda,t)\ E(\lambda)\ d\lambda}$$

where $S(\lambda, t)$ is the spectrum at the top of the cloud and $E(\lambda)$ the (erythemal) action spectrum. Continuing, we approximate the integral by a summation (omitting time arguments

for brevity):

$$\frac{UVD}{UVD_{CS}} \approx \frac{\sum_{\lambda=280}^{400} S_\lambda\ E_\lambda\ CAF_\lambda}{\sum_{\lambda=280}^{400} S_\lambda\ E_\lambda} = \frac{\sum_{\lambda=280}^{328} S_\lambda\ E_\lambda\ CAF_\lambda + \sum_{\lambda=328}^{400} S_\lambda\ E_\lambda\ CAF_\lambda}{\sum_{\lambda=280}^{328} S_\lambda\ E_\lambda + \sum_{\lambda=328}^{400} S_\lambda\ E_\lambda}$$

The sum is split up in the relevant wavelength ranges of the SICCS product. SICCS bands 1 and 2 correspond to wavelengths 283 - 328nm and 328 - 408nm respectively. Although the CAF is wavelength dependent, we assume now that within each band the wavelength dependency is weak and can be considered constant. We will see in section 6.2 that the wavelength dependency is indeed weak so that this is a reasonable assumption. Continuing further, in terms of SICCS bands:

$$\frac{UVD}{UVD_{CS}} \approx \frac{(S \cdot E)_1}{(S \cdot E)_1 + (S \cdot E)_2}\ CAF_1 + \frac{(S \cdot E)_2}{(S \cdot E)_1 + (S \cdot E)_2}\ CAF_2$$

Finally we can write CAF in terms of CAF_1 and CAF_2:

$$CAF = c \cdot CAF_1 + (1 - c) \cdot CAF_2 \tag{6.2}$$

where c is the constant[1] determining the contribution of each band. To find CAF, we need to find CAF_1 and CAF_2, and the contribution of the bands; c.

Cloud attenuation factors CAF_1 and CAF_2 are the (theoretical) ratios of cloudy to clear sky UV for a range of wavelengths. The available data sets do not contain (erythemally) weighted irradiances, but do contain total irradiance per band (the SDS). To relate the theoretical CAF to what is practically available, we assume the UV ratio to be equal to the corresponding SDS ratio:

$$CAF_i \equiv \frac{UV}{UV_{CS}}\Big|_i \approx \frac{SDS_i}{SDS_{i,CS}} \tag{6.3}$$

with $i \in \{1, 2\}$. This is the crucial assumption to represent the (theoretical) CAF by practically available quantities.

6.2 Band contribution

Clouds affect light differently depending on the light's wavelength. The data from the SICCS bands is subject to the same dependency. How clouds affect light of different wavelenghts is described in the following subsection. What this means for the bands is described in subsection 6.2.2.

6.2.1 Wavelength-dependent cloud effect

Constituents of the atmosphere affect light in different ways depending on the wavelength of the light. A simple example is the blue sky, caused by the fact that light of short wavelengths is scattered more than light of long wavelengths. The effect of clouds is also wavelength dependent, even though scattering in clouds is mostly wavelength independent; clouds are white. Light may hit the cloud at different angles. Light hitting the cloud at a large angle will traverse through more cloud than light coming from the cloud's plane normal. The (average) direction of the light hitting the cloud depends on how much it is scattered above the cloud, which *is* wavelength dependent.

6.2.2 Cloud effect in bands

The band contribution determines how much each band's CAF_i contributes to the eventual CAF (equation 6.2). We may expect a difference between CAF_1 and CAF_2 because of the

[1] Band contribution c varies, like the solar spectrum, with atmospheric conditions at the top of the cloud and is not an actual constant.

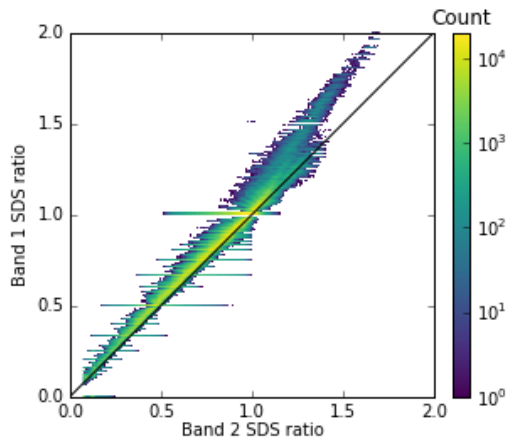

FIGURE 6.1: The SDS ratios of band 1 against those of band 2 in a 2D histogram. Points of the 12:00 GMT disc of 7, 17 and 27 August 2014 are included. Each disc yields about 10^7 points that are binned in 200∗200 bins. The black line indicates the 1:1 relation.

wavelength dependency described above. However, if this difference is small, we neglect it completely. To see if the difference between CAF_1 and CAF_2 is negligible, we study the respective SDS ratios (their practical representations, equation 6.3). The SDS ratios of band 1 from three day's full discs are plotted against SDS ratios from band 2 in figure 6.1.

Points of these three discs lie close to the 1:1 line. The Pearson's correlation coefficient of both ratios is 0.986. The difference between SDS ratios of band 1 and 2 is so small that we choose not to account for this difference in the model. Points from bands 1 and 2 will be treated equal for the curve fitting in the next section. Because bands 1 and 2 contain an equal amount of data points, a contribution constant $c = 0.5$ is inherently assumed.

6.3 Relating to SDS ratios

The SDS ratios needed to represent CAF_1 and CAF_2 (equation 6.3) are only available for a limited period. We would therefore like to find a relation between a long-term available quantity and the single-band SDS ratios so we can still represent the CAF on the long-term. Multiple quantities were tested, including the broad band SDS ratio which turned out to hold the best relation (i.e. largest correlation, smallest error) to the single-band SDS ratios. To find the relation between the single-band SDS ratios and the broad-band SDS ratio, a least squares fit is made. This fit is from thereon used to translate the broad-band SDS ratio to CAF_1 and CAF_2 to be inserted into equation 6.2.

As was concluded in section 6.2.2, there is no significant difference between bands 1 and 2, so data of both bands can be combined to have more points for the fitting procedure. Pixels from SEVIRI discs of noon on the 7th, 17th and 27th of August 2014 are used, yielding close to $6 * 10^7$ points. The single-band SDS ratios from bands 1 and 2 are plotted against the broad-band SDS ratio in figure 6.2a. The pattern appears curved, so a second order polynomial fit function is used. The resulting function is as follows:

$$y = -0.435\,x^2 + 1.348\,x + 0.095 \;\approx CAF_{UV} \tag{6.4}$$

where

$$y = \frac{SDS_{1+2}}{SDS_{1+2,CS}}$$

is the collection of all points from bands 1 and 2, and

$$x = \frac{SDS_b}{SDS_{b,CS}}$$

is the broad-band SDS ratio.

The error that is introduced from representing the single-band SDS ratios as a fit is related to the spread in the banded SDS ratios, and is computed as follows:

$$\sigma_{CAF} = \frac{\sigma_{1+2}}{\mu} \cdot y \tag{6.5}$$

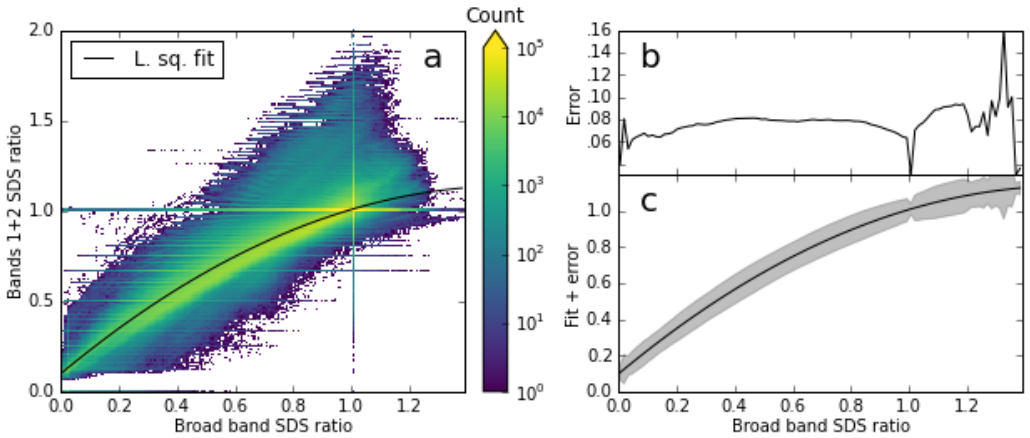

FIGURE 6.2: a) A 2D histogram of single-band and broad-band SDS ratios from multiple SEVIRI discs. The black line shows the least squares fit. b) The error as a function of broad-band SDS, in units of SDS ratio of bands 1 and 2. c) The fit plotted with the error added.

where σ_{1+2} and μ are the standard deviation and mean of the single-band SDS ratio respectively. Note that we neglected errors of individual points (i.e. assume they are not biased). Figure 6.2b shows the resulting error as a function of broad-band SDS ratio. This is computed by dividing the x-axis (broad band SDS ratio axis) into 100 bins on which the standard deviation and mean is calculated. The same error is shown as shaded area above and below the fit in figure 6.2c for a better perception of scale. The error does not seem to change significantly for different broad-band SDS ratios, except for where the broad-band SDS ratio is 1. We assume the error to be the mean error everywhere, except when the SDS ratio is 1:

$$\sigma_{CAF} = \begin{cases} 0.030 & x = 1 \\ 0.077 & x \neq 1 \end{cases} \tag{6.6}$$

6.4 Comparison of cloud masks

Using the newly available cloud information changes the final UV product in two ways:

1. The UVD is computed for a larger region
2. The cloud method is different (as described in previous sections)

We compare the old with the new product following the same two steps. It is easiest to compare the new cloud method to the old cloud method on the full disc. This is possible because the newly available data also includes a cloud mask. However, this cloud mask differs from the previously used cloud mask data due to different processing (Derrien et al. 2013, Greuell et al. 2013). Both cloud mask data sets are shown in figure 6.3.

In general there is good agreement between both cloud masks, but some differences can be found. The old mask includes pixels with a larger viewing angle than the new mask and thus has a larger disc. Moreover, some new cloud mask values differ from the old, often showing more 'cloudy' pixels where the old data set has 'contaminated' pixels. Other than that, there is good agreement and no large difference are expected in the resulting UV product. We can therefore compare the new cloud method, using SDS ratios, to the cloud mask on the full disc as representative for the old method. We expect differences in UVD between the old (cloud mask) method and the new (SDS ratio) method to be more significant than differences due to slight differences between old and new cloud masks.

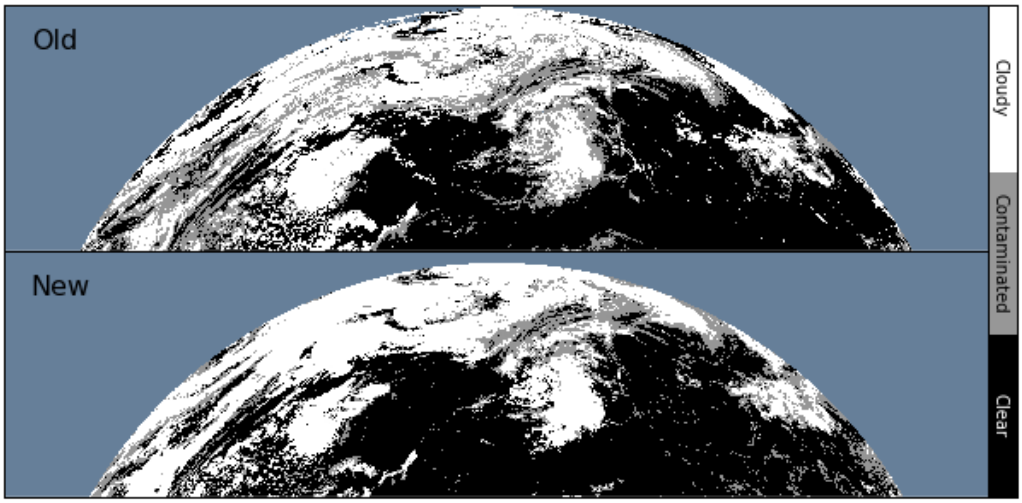

FIGURE 6.3: Different cloud masks of the same SEVIRI data set, showing only the northern part of the disc observed by the SEVIRI instrument (12:00 GMT, September 2nd, 2012). The old cloud mask data is only available for the shown region whereas the new data is available for the full disc (not shown here).

6.5 Comparison of methods

Changing from the cloud mask method (CMM) to the SDS ratio method (SRM) is not an obvious improvement, but rather a different approach. We can consider the quality of each method to determine which is expected to give the better result. The quality of cloud information from the CMM depends on:

- The accuracy of the SICCS cloud mask product
- The quality of the fit relating cloud mask to CAF
- The ability of a cloud mask to represent actual cloud cover

The quality of cloud information from the SRM depends on:

- The accuracy of the SICCS SDS product
- The quality of the fit to reproduce SDS ratios

The first points of both methods should be equal and no method is favoured on these points. The second point, related to the quality of the fitting methods, favours the CMM. Regardless of the errors related to the fits, the fit for the CMM is done with respect to actual observations, whereas the fit for the SRM is a relation between different model outputs. The third point for the CMM is the main reason for changing to the SRM. A cloudy pixel has a CAF in a range of possible values depending on the cloud physical properties, which is not represented by the CMM. With the SRM, we utilize such cloud properties using the SICCS algorithm, which is validated and tailored for computing cloud properties. The SRM should therefore better represent the CAF and is expected to better agree with measurements.

Regardless of the differences, both methods describe the same physical effect and should therefore agree to some extent. Figure 6.4 shows 2D histograms of UVD and CAF with either method on either axis, using data from September 2nd, 2012. From figure 6.4a we see that the majority of the points agree well, lying close to the 1:1 line. However, this is as expected since the UVD is determined by parameters other than the CAF that agree exactly between both methods. The sole effect from the CAF is shown in figure 6.4b. Most notable is the range of attenuation factors from each method. The CMM only allows CAF between 0.5 and 1, whereas the SRM allows CAF from about 0.1 and over 1. The SRM can be interpreted to distinguish different intensities of 'overcast' that the cloud mask method does not. The values over 1 can be interpreted as a sky albedo

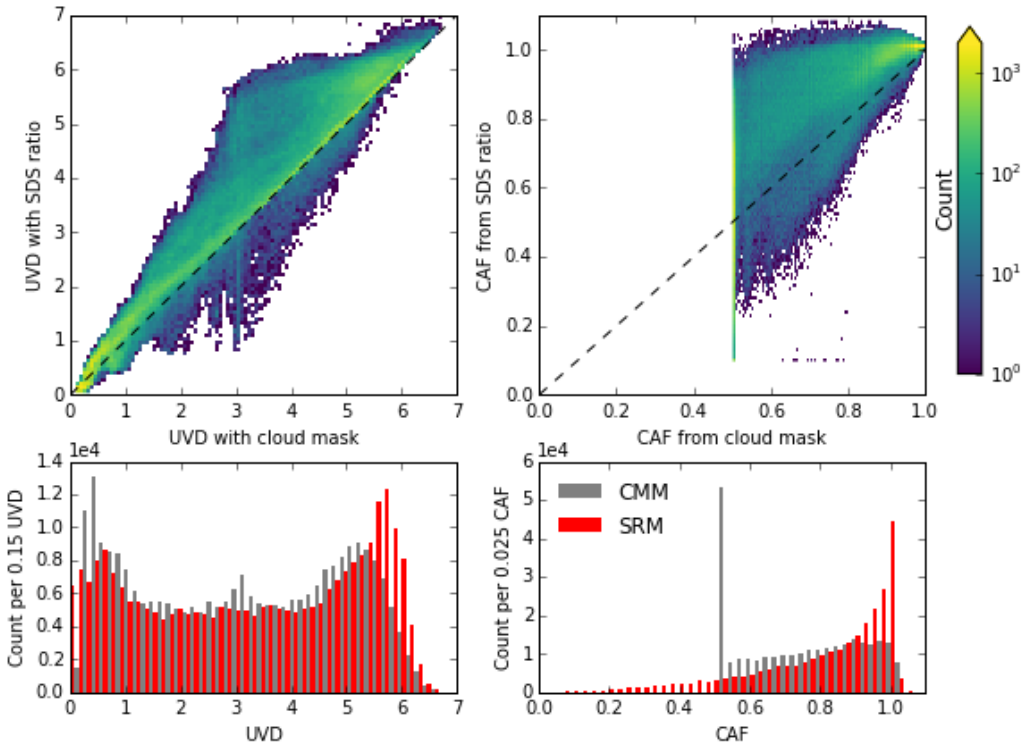

FIGURE 6.4: Density distributions in 2D and 1D to compare different cloud methods using data of September 2, 2012. a) Distribution of UVD calculated using the CMM (x-axis) and SRM (y-axis), and b) the corresponding CAF. c) The distribution of UVD using the CMM (grey) and SRM (red), and d) the corresponding CAF.

effect reflecting more light, but may also be an algorithmic effect related to aerosols (see discussion, section 6.6). The distribution of CAF from both methods is shown in 6.4d. A clear spike at $CAF = 0.5$ is shown for the CMM. Other values of CAF are more evenly distributed. The CAF distribution from the SRM shows an increasing amount of high CAF (i.e. thin clouds). There is a significantly higher amount of thin clouds using the SRM than when using the CMM, but clouds are also allowed to be 'thicker' (i.e. CAF below 0.5).

The UVD seems to be generally higher using the SRM than using the CMM. This is apparent from figure 6.4a, with a higher count of points lying to the top left of the 1:1 line. The distribution of UVD (figure 6.4c) shows where the differences are. The CMM generally has a higher count for intermediate UVD values (between $\sim 1 - 5$). The SRM shows the largest count in high UVD values. This is likely related to the increased amount of thin clouds. The high count at high UVD values for the SRM also indicate low-latitude conditions; such high UVD does not occur at high latitudes, regardless of clouds. The different cloud methods across the globe (or SEVIRI disc) can be seen in figure 6.5.

Clear differences between both methods can be seen around low latitudes. Both methods detect the same clouds (both data sets are from the same SICCS product), so the only differences are in their CAF. The UVD with CMM shows more spots of low values in the tropics than the UVD with SRM. However, these spots of low UVD reach the lowest values with the SRM. The significance of good cloud information is stressed by this figure. Public information institutes will be interested in potential dangers from high UVD values. Studies using UVD data may be interested in the occurrence of sudden low values due to thick cloud cover.

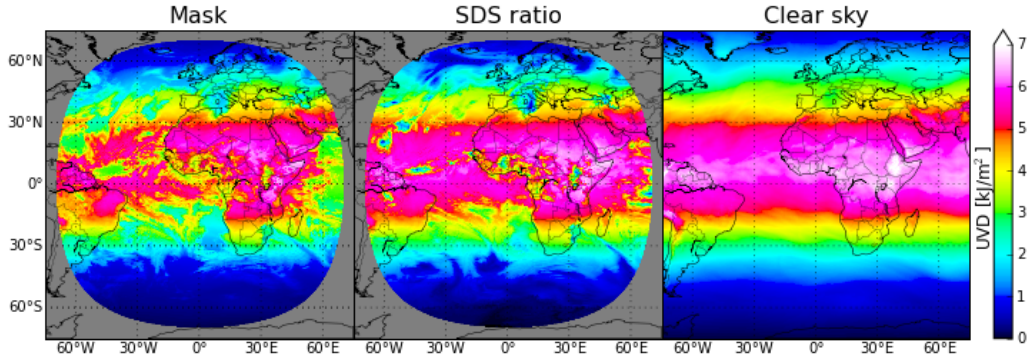

FIGURE 6.5: The UVD on September 2, 2012, computed using the CMM (first panel), the SRM (second panel) and cloud free conditions (third panel). Grey area is not observed by the SEVIRI instrument and contains no cloud data.

6.6 Discussion

Figure 6.2 and equation 6.4 prove the relevance of the described method. The broad-band SDS ratio from the long term available data set may arguably be used directly as the CAF. However, this is physically not as sensible as using the single-band SDS ratios: the broad band data represents the wrong wavelengths. Figure 6.2 and equation 6.4 show there are indeed differences between the broad-band and single band as their relation is not 1:1 (nor linear). In practice, this method will prove to be more convenient in the future. When the single-band data becomes available it can easily be implemented in the model on the physical principle discussed in this chapter.

Note that equation 6.4 and particularly figure 6.2 show the relevance of the method, but do not prove its quality. Figure 6.2a shows a large spread, indicating that in some situations the fit is very inaccurate. We also argued the use of a quadratic polynomial by saying the pattern looks curved. Although this seems somewhat simplistic, it is a sufficient argument for now. We are interested in finding a relation that when applied yields a small error without (too much) loss of generality. There is no reason to assume that the relation should be linear, so a quadratic curve may be sufficient. On the other hand, using a higher order polynomial for fitting may cause a loss of generality. A high order polynomial tends to follow specific curves in the pattern that may only appear on the day or month that the fit was made, but not at other times.

The order of the polynomial and parts of the fitting procedure may still be improved on. The fitting procedure could be narrowed down by splitting the histogram into different regimes and making separate fits for each regime. Perhaps using regimes qualified by aerosol properties or cloud phase may show clear distinctions in the histogram's pattern. There are many combinations of regimes, quantities and fitting functions to consider. There is certainly room for improvement regarding this fitting procedure.

Another point of discussion is the representation of the CAF by the available data. The crucial assumption to relate the CAF to available data is shown in equation 6.3, indicated by the approximate-sign. We state two reasons why this is only an approximation and why the CAF is not perfectly represented by the SDS ratio:

One reason for this is the difference in how transmission through clear and cloudy sky is computed. Aerosol effects are used if no cloud is present, which are otherwise neglected. Pixels with thin clouds and many aerosols may wrongly cause an increase in insolation with the addition of clouds. This partly explains why some SDS ratios (e.g. those shown in figures 6.1 and 6.2) have values above 1. However, a CAF over 1 is not considered a wrong value, as there are also physical effects that cause a CAF over 1. The 3D effect of clouds can cause higher insolation in the presence of clouds than in the absence of clouds.

Another reason is the difference in ozone data used for the SICCS and UV models. SICCS uses a climatology from MSR data (van der A et al. 2015) or MACC-II/CAMS data (Basart et al. 2016), whereas the UV model uses real time GOME-2 data (Eskes

et al. 2003). Small differences in total column ozone values cause small a discrepancy between the UV ratio and the SDS ratio that is relevant for the UV ratio.

Chapter 7

World-avoided scenario

The human species distinguishes itself from other animals with its superior intellect. Using their intellect, humans have thought up tools or systems to make life easier for themselves. Although the immediate effects are often obvious, like a car providing easy transport, other effects may not be as easy to understand. The destruction of ecosystems, for example, is a side effect for creating space for farmland. Another example is the emission of greenhouse gases and smog as a secondary effect of generating heat for carbon-fueled machines. The latter is a good example for the adverse effect on humans in particular from their own inventions. Building machines is good for human health as it keeps them from having to do heavy labour, but the emission of large amounts of particles and pollutants may cause respiratory problems and early death as happened during London's Great Smog of 1952 (Bell et al. 2004).

Another example, with more relevance for UV light, is the emission of ozone depleting substances (ODS). Since several decades before the 1970s, when concern of their ozone depleting properties started (Molina & Rowland 1974), chlorine-containing compounds were used in various applications. This ultimately led to the formation of the Antarctic ozone hole (Farman et al. 1985).

In this chapter, a specific human-induced scenario will be analysed. The ozone distributions as calculated by Chipperfield et al. (2015) provide us with such a scenario. These ozone distributions would have been present in the real world if there were no Montreal Protocol, an international treaty to ban substances that destroy ozone, signed in 1987.

We first present how the ozone data by Chipperfield et al. is applied for our study (section 7.1) and we discuss one of their results, with emphasis on the effect on UVD (section 7.2). We then pose two questions that are answered in the sections thereafter. Finally, we take a step towards explaining the relevance of the Montreal Protocol on human health (section 7.5).

7.1 Method: The ozone fields

A global total column ozone data set has been constructed from multiple satellite instruments that have monitored ozone since 1970 (van der A et al. 2015). This data set will be referred to as the multi sensor reanalysis (MSR) data set. The MSR data set will represent our 'current world' data set. The 'world avoided' (WAV) data set will be constructed from the MSR data with a factor applied that is derived from the 'no Montreal Protocol' (NoMP) by Chipperfield et al. and their control run (MP).

The data sets by Chipperfield et al. are given on a grid that differs from what we are interested in. Their spacing between data points is about 2.8125 degrees in each direction, and both poles are absent. Information on the poles is acquired by taking the mean of all surrounding points. The data is then transferred to our 0.25° grid by linear interpolation. The ratio between the NoMP data and the control run is then multiplied by the MSR ozone to get the WAV ozone (equation 7.1).

$$O_{3_{WAV}} = f_{O_3} \cdot O_{3_{MSR}} \tag{7.1}$$

where

$$f_{O_3} \equiv \frac{O_{3_{WAV}}}{O_{3_{MSR}}} = \frac{O_{3_{NoMP,regrid}}}{O_{3_{MP,regrid}}} \tag{7.2}$$

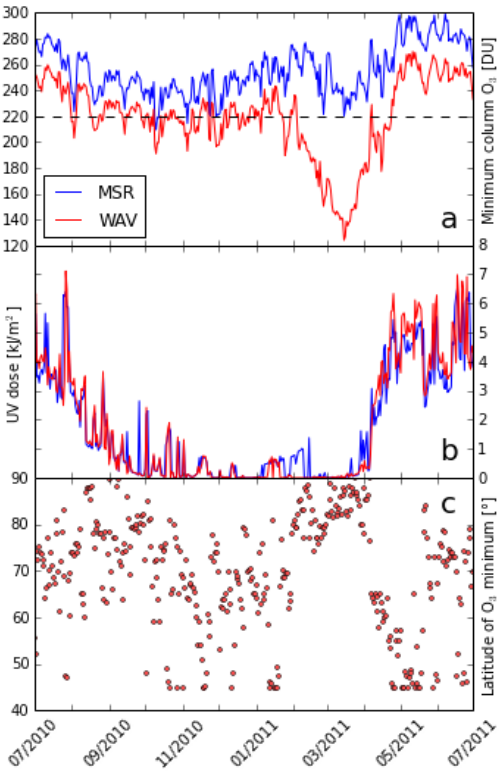

FIGURE 7.1: Minimum column ozone values and their corresponding UVD and latitudes. a) Daily minimum column O_3 values in the MSR and WAV scenarios, including only points above 45° latitude. b) The UVD at the location of the ozone minimum. c) The latitude at which the ozone minimum of the WAV scenario occurred.

The resulting ozone fields are then used to calculate the erythemal UV dose and index. This is done for the years from 1978 up to and including 2012, the the same time period modelled by Chipperfield et al. The calculation is performed using the cloud free model as described in previous chapters. The 31st of December 2012 is missing from the MSR data set. This has been accounted for by using a copy of the 30th of December 2012 in its place.

7.2 The UV story

During the northern hemisphere spring of 2011 (March and April) very low ozone values were observed at high latitudes and the polar region. Total column ozone values were so low that ozone hole status (total column $<$ 220DU) was almost achieved. In the WAV scenario, a deep Arctic ozone hole occurs with values well below 150 DU. This ozone hole exists for about 3 months and covers a major part of Scandinavia. This is accompanied by a large relative increase in UVI; over 50% in the world-avoided scenario of Chipperfield et al. The UVD shows a similar increase in our WAV scenario.

A 50% increase of UVD could pose a serious health threat in some parts of the world. The UVD is directly related to some health effect on humans. A 50% increase in erythemal UVD would therefore increase the rate at which the skin reddens by 50%. However, the low amount of solar irradiance in late winter/early spring at the poles results in a low UVD, regardless of ozone. The location at which the ozone depletion occurs is therefore important. A significant health effect may arise when the ozone depletion reaches lower latitudes.

The minimum ozone values during the would-be ozone hole event of 2011 are shown in figure 7.1a. This figure is similar to one of the figures by Chipperfield et al., but there are minor differences. This is due to differences in the methods: Chipperfield et al. modeled two scenarios providing daily ozone values. We received monthly means from these daily values from which f_{O_3} is derived. To produce daily data we interpolated these monthly mean factors in time and applied these to the daily MSR data.

In figure 7.1b the UVD is plotted at the location of the ozone minimum. The WAV UVD is near zero for most of the ozone hole event. We see that extreme values in ozone are

not necessarily accompanied by extreme values in UV index or dose. This can be explained from figure 7.1c. The minimum ozone values during the ozone hole event all occur at very high latitudes. The solar zenith angle, which is directly related to the latitude, is close to 90° at this time of year. The large solar zenith angle at the ozone minima strongly limits the amount of UV irradiance at the surface, resulting in a low UVD. Figure 7.1c shows latitudes of the ozone minima in the WAV scenario specifically.

The UV irradiance has a certain spatial pattern, with high values towards the equator and low values in the polar region. As we have seen in figure 7.1, this is the cause for low UVD at the ozone minima. There is also a certain spatial pattern regarding f_{O_3}: Chipperfield et al. found that ozone depletion is most prominent at the poles. We may therefore expect a large relative increase in UV at the poles. The amount of available sunlight and the ozone depletion follow a similar spatial pattern but counteract each other. We can pose two questions:

- How does the change in UV relate to the change in ozone?
- Where can we find the largest change in UV?

Regarding the first question, we explain our findings in section 7.3 by examining the spatial pattern that both available sunlight and ozone depletion exhibit. The second question is answered in section 7.4, stressing the combined effect of the parameters (solar zenith angle and ozone).

7.3 Comparison of UV and ozone factors

Comparing both scenarios, we find that in absence of the Montreal Protocol, total column ozone levels have solely decreased from 1987 onward. This means that at each location $f_{O_3} < 1$. We should find similar behavior in the UVI factor:

$$f_{UVI} \equiv \frac{UVI_{WAV}}{UVI_{MSR}}$$

We expect that $f_{UVI} > 1$, larger for smaller f_{O_3}. In this section we study how f_{UVI} increases as f_{O_3} decreases by plotting the corresponding factors and considering the model equation. For the rest of this section, we will study the UVI instead of the UVD. The UVI is very similar to the UVD in global pattern and the information it represents. The UVI, however, is mathematically less complicated which is why we use it here.

The scatter plots in figure 7.2 (a and c) show changes between scenarios in UVI in relation to changes in ozone for single days. A relation is visible in the scatter plots: Moving from the 1,1-point towards lower f_{O_3}, the f_{UVI} increases nearly linear. The linear behavior continues to and below $f_{O_3} \approx 0.95$, where a branch starts to deviate towards lower f_{UVI}. For lower f_{O_3} most points deviate from the linear relation towards lower f_{UVI} forming another branch that spreads through a larger portion of the plane. The amount of points that follow the linear behavior include about two-thirds of the total amount of points. However, the amount of points gives a skewed picture of the surface fraction, as the surface near the poles is over-represented with respect to the surface near the equator. Most of the points following the linear behavior lie away from the poles, and therefore represent a larger than two-thirds portion of the planet.

From the existence of the branches we can see there are conditions where the UVI is less dependent on (changes in) ozone. The points in these limbs lie close to the pole; points in the tip of the limb are roughly closest to the pole and points at the base of the limb are further from the pole. According to the parametrization of the UVI (a function of solar zenith angle and total ozone column, equation 2.3 (Allaart et al. 2004)) we can regard the pole as a limit.

For large solar zenith angles (i.e. close to the poles, depending of the time of the year), the first term of equation 2.3 becomes negligible, simplifying the equation:

$$\frac{UVI}{UVA} \approx \frac{H}{TO} + J$$

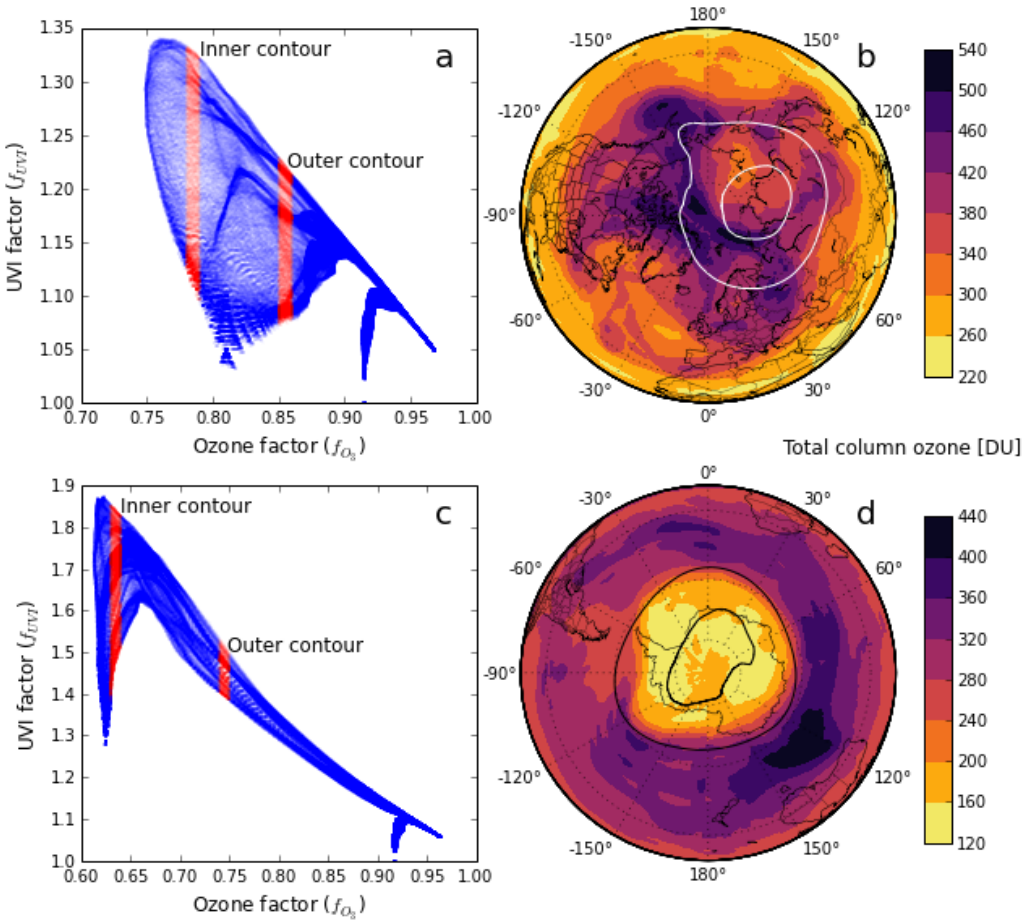

FIGURE 7.2: The UVI and ozone factors, and MSR ozone on the spring pole in 2008 on March 21st (a and b) and September 21st (c and d). a) Scatter plot of f_{UVI} vs. f_{O_3}, b) The MSR ozone data in color and some f_{O_3}-contour lines corresponding to the red sections of a. c/d) Similar to a/b where spring is now on the South Pole.

The UVA is independent of ozone, and thus equivalent in each scenario. We can insert f_{UVI} and f_{O_3}:

$$f_{UVI} = \frac{UVI_{WAV}}{UVI_{MSR}} \approx \left(\frac{H}{TO \cdot f_{O_3}} + J\right) \Big/ \left(\frac{H}{TO} + J\right)$$

Which can be written as:

$$f_{UVI} = \frac{1-a}{f_{O_3}} + a \tag{7.3}$$

with

$$a = \frac{J}{\frac{H}{TO} + J}$$

From equation 7.3 we see that f_{UVI} has two terms; one dependent and the other independent of f_{O_3}. The value of a depends on the total column ozone value; it increases as TO increases. If a is close to one (high ozone values), f_{UVI} is less dependent on f_{O_3} than if a is small (low ozone values). Near the poles (and thus in the high SZA limit), the total column ozone value is highly variable in space, meaning that dependency of f_{UVI} on f_{O_3} also varies a lot. Regarding f_{O_3} at the poles, we find that there is a - global or local - minimum here (i.e. the largest difference between the WAV and MSR scenarios).

We can now explain the branch patterns in the scatter plot. Comparing the two branches, the largest occurs at the spring pole where the ozone varies most and f_{O_3} is at its global minimum. The smallest limb occurs at the autumn pole where the variation is relatively large and f_{O_3} is at a local minimum. The local minimum at the autumn pole is

rather shallow, meaning that it only spans a narrow range of f_{O_3} values, explaining the sharpness of the branch. The minimum at the spring pole is deeper, and thus spans a larger range of f_{O_3} values. Together with the larger ozone variation, the branch containing points of the spring pole is much larger in both f_{O_3} and f_{UVI} extent.

Following this reasoning we can also understand why some years/days show more spread than others, and especially the difference between each hemisphere's spring. In other words, we can explain why figure 7.2a and c look different. The spread in f_{UVI} occurs when an f_{O_3}-contour crosses many different ozone values. A large ozone value causes f_{O_3} to have a small effect on f_{UVI}, leaving it close to unity. A small ozone value causes f_{O_3} to strongly influence f_{UVI}, making it deviate from unity. The relatively small spread on a South Pole spring with respect to a North Pole spring is related to the more symmetric nature of South Pole meteorology (figures 7.2 b and d, as one example). f_{O_3}-contour lines are more often centered on the South Pole, and so are the total column ozone values. Following an f_{O_3}-contour, one will encounter fewer different ozone values and thus fewer different f_{UVI} values.

We have shown in this section how surface UV irradiance is affected by a particular change in ozone. There is a spatial pattern in f_{O_3} and in f_{UVI} as a result, with the majority of the globe affected by the highest f_{O_3} values (having the smallest effect on f_{UVI}). Lower f_{O_3} values tend to occur towards the poles; the spring pole in particular has very low f_{O_3} values present. We also found that the largest change in ozone does not necessarily cause the largest change in UVI, because of the dependency on SZA and ozone. These dependencies are studied in more detail in section 7.4.2.

7.4 The largest change

In this section we study the difference between the MSR and WAV scenarios and look for the largest change in UVD in particular. To find the largest change in UVD, it is not sufficient to look for the largest ozone difference, as we saw in section 7.2. One of the results presented in the paper by Chipperfield et al. is the small effect of the Montreal Protocol on the ozone in the equatorial region. Both relative and absolute effects are small; a reduction of ozone of around 5% or less than 20 DU in the most recent years. The differences over the poles can easily exceed 20% or 80 DU in recent years, varying with seasons and from pole to pole (the difference on the South Pole is generally much larger than on the North Pole). However, sunlight is much more abundant in the equatorial region than in the polar region. Clearly both pole and equator govern constructive (i.e. respectively, large ozone depletion/much sunlight) and limiting (i.e. little sunlight/small ozone depletion) conditions for UV irradiance. Perhaps the largest change UV irradiance is found somewhere in between.

7.4.1 Finding the largest change

Finding the largest change in UV requires a different approach, regardless of the ozone values. Values of the UVD at a certain time of year do not tend to vary much on a single latitude, with the exception of mountain ranges and occasional unusual ozone behavior. We can therefore simplify our data by looking at zonal means. We then look at variations of each monthly mean through the years. An example of March is shown in figures 7.3a/b. Graphs for different months are found in the appendix.

Let us first consider the relative difference (figure 7.3a). We see that the effect of the Montreal Protocol on UV has been small in the first 10+ years, with less than 4% increase of UVD up to the year 2000. By 2012, an increase of over 16% is observed at mid to high latitudes. The would-be ozone hole of 2011 (discussed in section 7.2) is clearly visible as well, reaching a maximum increase of about 35%.

The month March is chosen as an example (figure 7.3) because it clearly features two types of behavior we would like to discuss. First, the relative UVD pattern in March shows that the maximum relative effect is neither found at the equator, where the solar zenith angle is smallest (i.e. most insolation), nor at the pole, where the change in ozone is largest. The same conclusion would follow when considering the absolute UVD effect of the Montreal Protocol, although the absolute change seems to be more focused on the

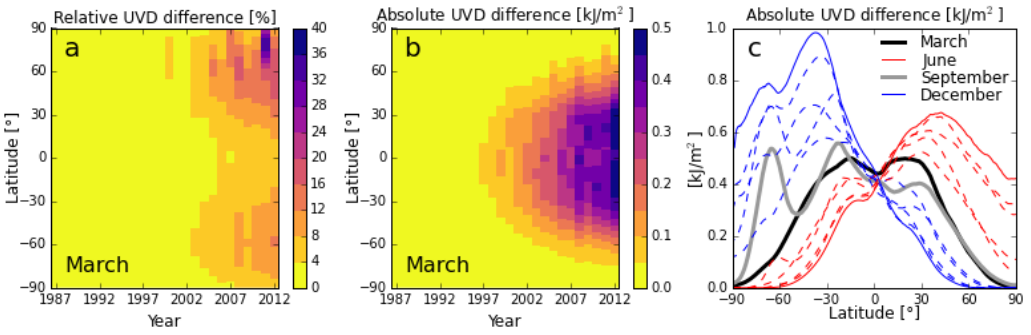

FIGURE 7.3: Zonal monthly means of UVD difference between WAV and MSR scenarios. a) The relative difference (WAV/MSR -1) of all Marches since the Montreal Protocol has been in effect. b) The corresponding absolute difference (WAV - MSR). c) Absolute differences for each month of 2012; blue dotted lines are Oktober, November, January and February; red dotted lines are April, May, July, August.

equator. This is because a small relative change where the absolute (MSR) ozone values are already high still yields a moderate absolute change in UVD. Nevertheless, the largest absolute UVD difference is rarely located at the equator. This is shown for multiple months in figure 7.3c. The months during which solstice or equinox occurs have been highlighted with continous and/or thicker lines. The maximum of each month seems to move with the overhead sun and is located around 30° north or south, depending on the season.

The second type of behavior well illustrated in March is the would-be ozone hole of 2011. During this year, a clear signal in the relative difference is visible around 70-80° north (figure 7.3a). A similar signal is visible in the absolute difference (figure 7.3b), but it is much less dramatic. Only slightly higher values at latitudes 60° and up are observed.

It is arguable which type of difference (relative or absolute) is more important for human health. The relative difference is intuitively easy to interpret; if the UVD has risen by 25%, you will burn 25% faster. However, a 25% increase may be meaningless if the UV dose was very low to begin with. A more definite answer to this question will be presented in section 7.5.

7.4.2 Calculating the largest change

As a rule of thumb, moving towards higher latitudes means the UV index or dose decreases due to increasing solar zenith angles. However, there are numerous exceptions to this rule. Variations in ground elevation, albedo and ozone distribution can cause local increases in UV irradiance towards higher latitudes. The increased day length also contributes to increase the UVD specifically. To find these local increases and ultimately the largest change, we study the UVI. We choose the UVI over the UVD because of its mathematical simplicity, and thus the day length effect is not accounted for. We simplify the UVI by ignoring the effect of surface albedo and ground elevation. These parameters are static and do not affect the behavior we are studying. Although both (generally) increase the UVI, they are not the *cause* for unusually high values. The resulting UVI is a function of solar zenith angle and total column ozone only.

The total column ozone changes due to absence/presence of the Montreal Protocol. We can look at the effect on ozone in two ways:

1. For a particular position, the local ozone value changes with changing scenarios.
2. For a particular ozone value (or contour), its position changes with changing scenarios.

The second point is particularly important during the Antarctic ozone hole season. The maximum change in ozone occurs around 60°-70° latitude, not on the pole. This can be interpreted as the ozone hole expanding rather than deepening.

The simplified UVI lends itself well to study both effects. Of course, the UVI is not a function of position but of solar zenith angle. We therefore consider only equinox days

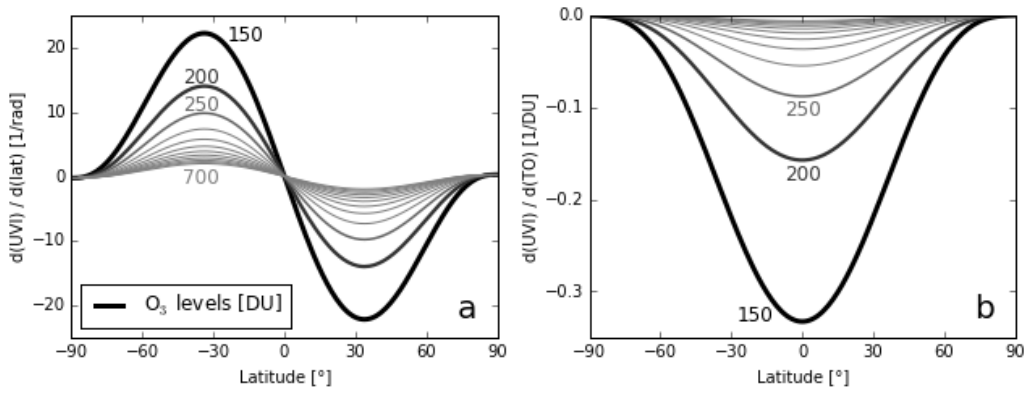

FIGURE 7.4: Partial derivatives of the UVI as a function of latitude with respect to; a) latitude (a proxy for solar zenith angle during equinox), and; b) total column ozone. Each line represents the function for a certain ozone level. Levels are separated by 50 DU.

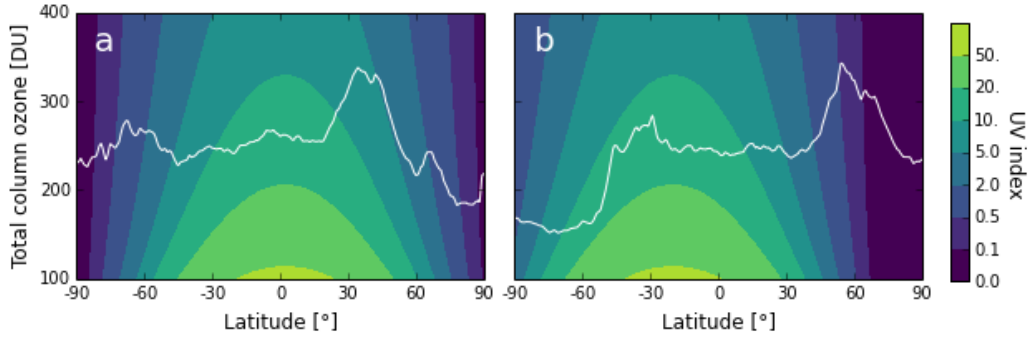

FIGURE 7.5: Ozone distributions (white line) of the WAV scenario as trajectories across UVI fields (coloured contours). a) The ozone distribution along the longitude through Oslo, Norway (centered on 10.625°E) on March 29th, 2011. b) The ozone distribution along the longitude through Ushuaia, Argentina (centered on 68.375°W) on November 20th, 2011.

first, so a 0° solar zenith angle coincides with the 0° latitude (the equator). To see how a change in total column ozone or position (or solar zenith angle) affects the UVI, we can take their respective partial derivatives. The derivatives of UVI as a function of latitude, at different values of total column ozone, are shown in figure 7.4.

From these simple derivatives we can largely understand how the UVI is affected by changes in ozone at different locations. A decrease in total column ozone, which happens when going from the MSR to the WAV scenario, will increase the UVI more over the equator than over the poles. This is shows as an (upside-down) peak in figure 7.4b. Displacing an ozone value along latitudes will change UVI values strongest near mid latitudes as this is where the peaks occur in figure 7.4a. Note that this does not mean that displacing a (hypothetical) equatorial ozone hole from -5° to +5° latitude hardly changes the UVI value at either location - it does, according to figure 7.4b. It means that the value inside the hole remains unchanged.

These simple partial derivatives provide rules of thumb for what kind of ozone changes cause what type of changes in UVI. We can extend our analysis to determine what type of ozone distributions cause maxima in UVI. To do this we want to know how the total column ozone affects the UVI at particular solar zenith angles. This is visualized for real-world ozone distributions in figures 7.5a and b. UVI values are plotted as contours in the latitude-ozone plane, representative for the time of year when the ozone distribution occurred. The ozone distribution along a specific longitude is shown in white; the trajectory through UVI values along a longitude.

By plotting the ozone distribution over the UVI values (figure 7.5), we can recognize where UVI maxima occur. Wherever the distribution, when moving towards a pole, dips downward steeper than the contours, it crosses the UVI contours towards higher UVI

values. This would imply an increasing UVI with increasing latitudes (away from the equator). This crossing to higher UVI values happens when the slope of the distribution (β) is larger than the slope of the contours (α) on the southern hemisphere, or when $\beta < \alpha$ on the northern hemisphere (that is, a larger negative angle, thus 'less than'). For angles $\alpha, \beta \in (-90°, 90°)$ we can also write the criterion (on the northern hemisphere) as:

$$\tan\beta < \tan\alpha \tag{7.4}$$

or on the southern hemisphere as:

$$\tan\beta > \tan\alpha \tag{7.5}$$

The slopes differ per latitude (ϕ), and can therefore be written as a function of latitude. The tangents of the slopes result from derivatives of the distribution w.r.t. solar zenith angle, and the UVI w.r.t. solar zenith angle and total column ozone.

On the northern hemisphere this looks as follows:

$$\tan[\beta(\phi)] = \frac{\partial TO}{\partial \phi} \qquad \tan[\alpha(\phi)] = \left.\frac{-1 \Big/ \frac{\partial UVI}{\partial TO}}{1 \Big/ \frac{\partial UVI}{\partial SZA}}\right|_{\phi}$$

And on the southern hemisphere:

$$\tan[\beta(\phi)] = -\frac{\partial TO}{\partial \phi} \qquad \tan[\alpha(\phi)] = \left.\frac{1 \Big/ \frac{\partial UVI}{\partial TO}}{1 \Big/ \frac{\partial UVI}{\partial SZA}}\right|_{\phi}$$

On both hemisphere the criteria (equations 7.4 and 7.5) become:

$$\frac{\partial TO}{\partial \phi} < -\left[\frac{\partial UVI}{\partial SZA} \Big/ \frac{\partial UVI}{\partial TO}\right]_{\phi}$$

which can be written more aesthetically appealing as:

$$\gamma > 1 \tag{7.6}$$

where

$$\gamma = -\frac{\partial TO}{\partial \phi} \Big/ \left.\frac{UVI_{SZA}}{UVI_{TO}}\right|_{\phi} \tag{7.7}$$

with subscripts denoting derivatives.

The parameter γ is a useful tool to classify the ozone field with respect to the UV index. A value larger than one indicates increasing UVI towards the poles. Directly poleward of where γ is larger than one, a local maximum is found. The denominator in equation 7.7 goes to zero below the overhead sun and we get very large spikes here. This is a physical result; the equatorial region is full of tiny local minima as the smallest ozone variation may cause one. However, this is not what we want to emphasize, so we will weight γ with a normalized absolute sine function; zero where the sun is overhead, and maximal at 90 degrees towards the north and south. This may seem very arbitrary; which it is, but it will better emphasize maxima at latitudes that are not likely to govern maxima - unless the ozone distribution contains particularly strong gradients, as happens during very deep ozone holes, or low-latitude ozone holes. The criterion of equation 7.6 is still valid, but when applying the weighting function we prefer a more intuitive criterion:

$$\gamma > 2/\pi \cdot |\sin(\phi - \phi_{sol})|^{-1}$$

where ϕ and ϕ_{sol} are latitude and the latitude of the overhead sun respectively.

Let us now see how γ performs on actual ozone distributions. The specific ozone distributions of figure 7.5 were chosen because they were related to extraordinary events. The ozone distribution in figure 7.5a occurred during the would-be northern hemisphere ozone hole of 2011 discussed in section 7.2. The ozone distribution of figure 7.5b occurred when an elliptic Antarctic ozone hole caused high UVI values over the south tip of South America. The northern hemisphere ozone hole did not cause a UVI maximum whereas the elliptic Antarctic ozone hole did. The γ should show the difference. For each event, γ, the ozone distribution and a map is shown in figure 7.6.

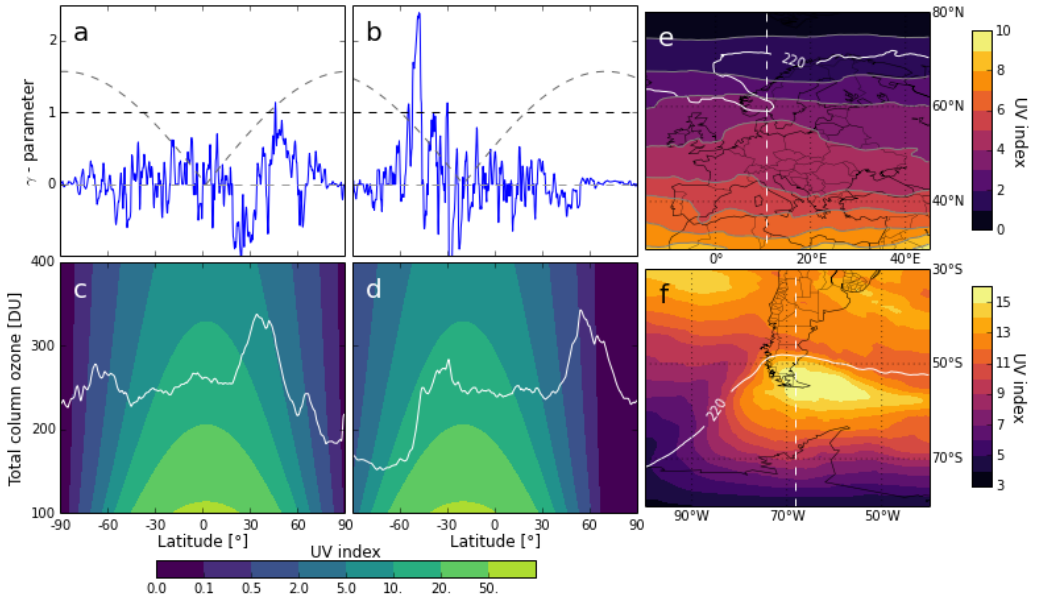

FIGURE 7.6: γ - parameters and corresponding ozone distributions and maps. a) γ on 10.625°E on March 29th, 2011. The gray dotted lines shows the weighting function that is applied. b) γ on 68.375°W on November 20th, 2011. c/d) Duplicate of figure 7.5a/b. e/f) UVI values on the world map on days corresponding to a/b. The 220 DU ozone contour is shown in white.

The ozone distributions in figures 7.6c/d look similar but mirrored. Both decrease steeply towards the spring pole. However, the UVI values on the map of figure 7.6e show a very different pattern from those in figure 7.6f. Plots of γ show a clear difference. The decrease of ozone towards the south pole (figure 7.6d) is paired with a (weighted) γ well over 1 (figure 7.6b). The decrease in ozone towards the north pole in March 2011 is paired with a peak in γ that does not exceed 1, but is much wider than most other peaks (figures 7.6a/c, between 40°-60°N). The peak in figure 7.6b (at 50°S) implies UVI contours are crossed towards high UVI values while moving poleward, causing a UVI maximum. Figures 7.6d and f confirm this. A γ of (close to) one means that the ozone distribution follows the UVI contours, which we see in figure 7.6c. A UVI maximum is not reached, but instead a certain UVI value persists over multiple latitudes, causing a widening of UVI contour lines on the map of figure 7.6e.

To conclude, we have found a successful way to classify ozone fields in which elevated UVI values occur at high latitudes. Finding the location of a local UVI maximum is one result. Other ways in which the UVI is elevated due to features in the ozone distribution are also found, like the persistence of a low-latitude UVI to higher latitudes. This helped to explain the difference between the Arctic ozone depletion event in March 2011 and the elliptic Antarctic ozone hole in November 2011 regarding the effect on the UVI.

7.4.3 At the largest change

Finally, we present the change in UVD through the years in both our scenarios. We have observed that changes in UVD mostly occur around mid latitudes. We have confirmed this by studying the equations of the model for the UVI, which is closely related to the UVD. We will present the course of monthly mean UV doses throughout the years at different locations; both inside and outside the 'maximum'. Some will be shown here, more can be found in the appendix.

Consider figures 7.7 and 7.8. These figures show the course of monthly mean UVD in both scenarios for the years since the Montreal Protocol, in De Bilt (52.12°N, 5.2°E) and Ushuaia (54.8°S, 68.3°W). The behavior in the WAV scenario is very similar to that in the MSR scenario, but with a steeper trend. High UVD in the WAV scenario only occur when paired with a similarly high value in the MSR scenario. No 'new' types of behavior arise.

Furthermore the seasonal variability is clearly visible (as both De Bilt and Ushuaia lie far from the equator) and also the relevance of summer compared to winter. The UVD are low in winter, in either scenario, and thus the winter is not the time of interest regarding the effect of the Montreal Protocol.

This does not imply that the Montreal Protocol has not affected winter UVD, or seasonality in general. The UVD in the MSR scenario at each time corresponds to a UVD in the WAV scenario at a different time. This effectively lengthens the summer in terms of UV irradiance. UVD values at a specific location in the MSR scenario are found at higher latitudes in the WAV scenario. Thus there are both temporal and spatial shifts in UVD behavior due to an absent Montreal Protocol. Such shifts may be important for the health of ecosystems (Häder et al. 2007) or plant growth in general (Giese 2013, Zuk-Golaszewska et al. 2003) which are generally bound to a certain spatial extent, or temporal extent due to the growth season.

The zonal monthly mean of June 2012 is plotted against latitudes in figure 7.9a. The solstice month of the northern hemisphere is chosen because it has the largest displacement effect and the UVD also decreases monotonically towards the pole. This is not the case for the southern hemisphere solstice month because of the Antarctic ozone hole. The graph in figure 7.9b shows the displacement: For a UVD at any latitude from the MSR graph (figure 7.9a), move along the latitudes (horizontally) towards the WAV graph; the distance moved is the displacement. It features a sharp peak that corresponds to the maximum UVD in the MSR scenario. The dotted line in figure 7.9a indicates a range of latitudes where UVD values occur that do not occur in the MSR scenario (regarding the zonal monthly mean). The extent of this range is given by the peak of figure 7.9c. This is a little over 30° latitudes for this month. Other months (not shown) may show smaller extents; around 20 - 30°. The mean displacement to the north of the UVD maximum is about 9°.

Figures 7.9d, e and f show the displacement in time between UVD in the MSR and WAV scenarios for De Bilt. A least squares fit assuming a cosine function is constructed from which the displacements (figures 7.9e and f, black dashed line) are calculated. This is convenient as we are interested in the seasonal variation, not day to day variations. Furthermore, these figures contain similar information as figures 7.9a, b and c. Figure 7.9f shows how much longer one experiences UVD values over a certain level in the WAV scenario, with respect to the MSR scenario. The peak represents how long 'new' values will be present (values that did not occur in the MSR scenario). Figure 7.9e shows in more detail the temporal displacement at each latitude, but is less informative than figure 7.9b is for spatial displacement due to its near-symmetry. The peaks of the MSR and WAV fits do not fall on the same day (27/6 for MSR, 25/6 for WAV), causing the slight asymmetry in the graph.

Suppose now that life anywhere solely depends on the amount and intensity of UV irradiance and reaches equilibrium within a month. Spatially, this means about a quarter of the planet is covered by new ecosystems not present in the current world, and current ecosystems on the northern hemisphere are found 9° further north. Temporally, this means the growth season is be lengthened. However, plants also die faster due to increased UV damage. They may evolve (within a month) to something different or be replaced by plants that occurred closer to the equator. Of course, this is a very unrealistic assumption, but investigating the detailed effects of these displacements is out of the scope of this thesis.

Table 7.1 lists some properties of the data by location. As stated in the previous sections, the UV effect is indeed maximal around mid latitudes for most locations. Particularly, the maximum month's trend is highest for locations near mid latitudes. This may not be true for annual trends; we saw in figure 7.3 that maxima occur near the mid latitudes, but only per month. The mid latitudes experience much lower values during winters. The effect near the equator is always moderately high, and thus the annual trend may have increased most near the equator. Regarding table 7.1, we can see that near the equator the difference between annual trends (i.e. Difference WAV-MSR trend, fifth column) is higher than those in mid latitudes, even though the maximum is often much less. This tells us that the Montreal Protocol has had a significant effect in all parts of the world, but is expressed different at different latitudes.

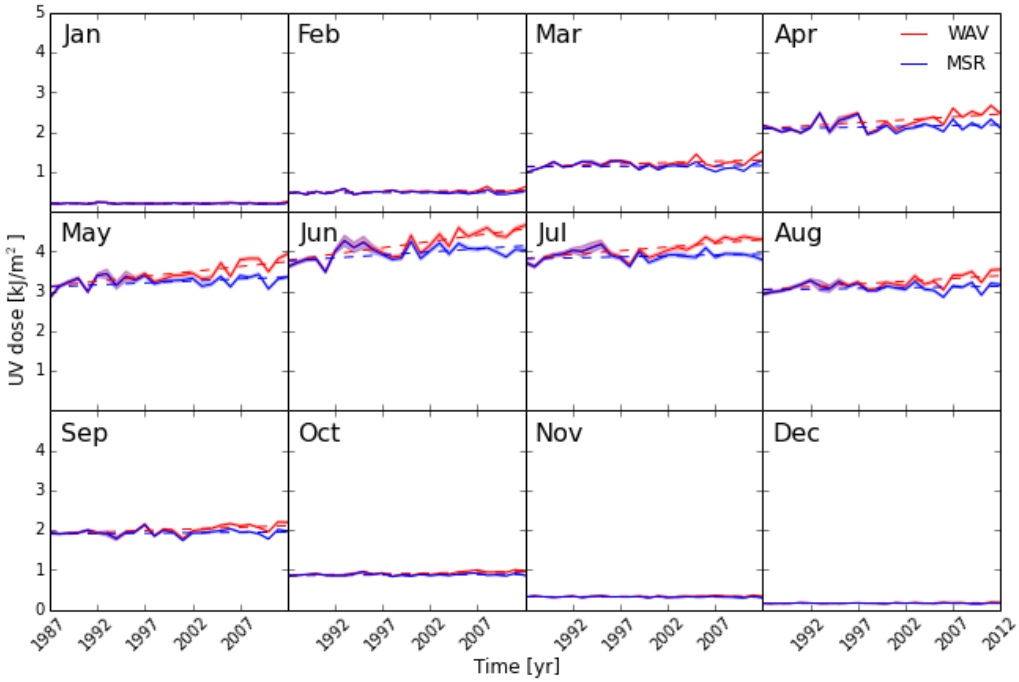

FIGURE 7.7: Monthly mean UV dose values in De Bilt, for each month since the Montreal Protocol (1987). The WAV and MSR scenarios are shown in red and blue, respectively. The shaded area is the monthly average UVD error.

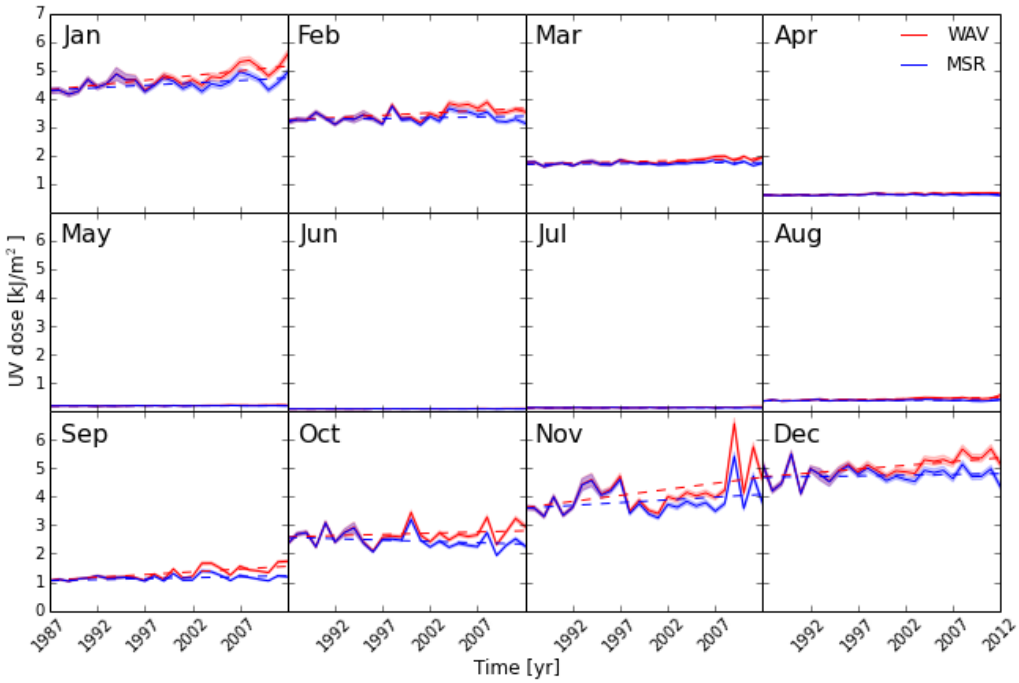

FIGURE 7.8: Monthly mean UV dose values in Ushuaia, for each month since the Montreal Protocol (1987). The WAV and MSR scenarios are shown in red and blue, respectively. The shaded area is the monthly average UVD error.

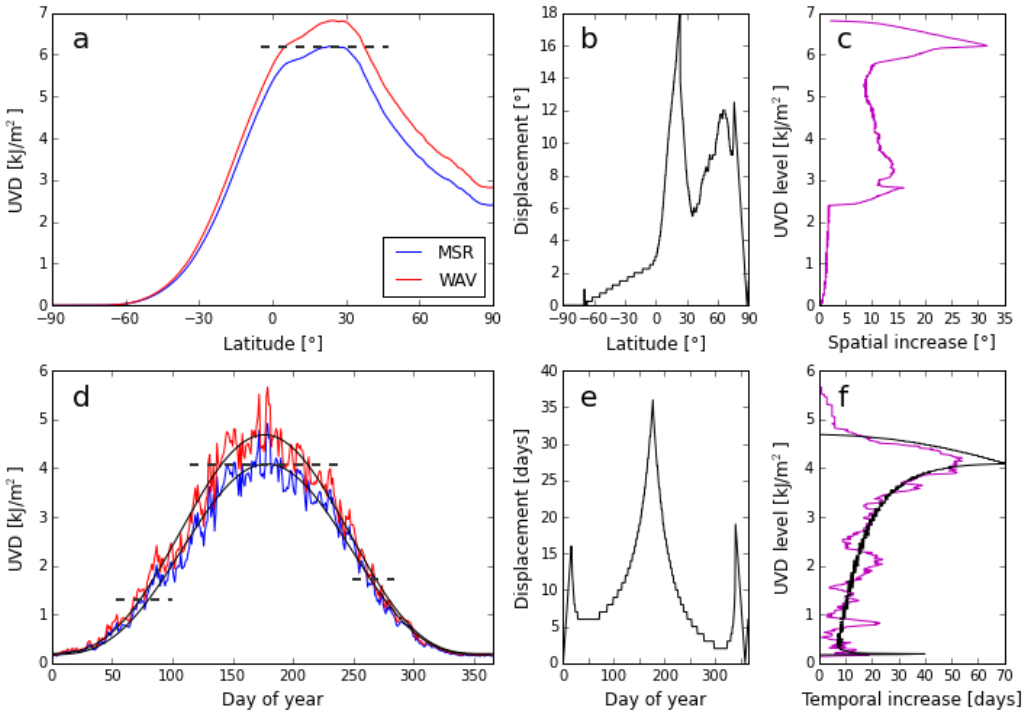

FIGURE 7.9: UVD in both scenarios and their corresponding displacement in space and time. a) The zonal monthly mean UVD of June 2012. The dotted line indicates where UVD values occur in the WAV scenario that did not occur in the MSR scenario. b) The spatial displacement (see text) of a. c) The difference between the number of latitudes where the UVD exceeds a certain level between both scenarios. d) The course of the UVD through the year 2012 in both scenarios for De Bilt. e) The temporal 'displacement' of d. f) The difference between number of days where the UVD exceeds a certain level between both scenarios (purple) and their fits (black, dashed).

To summarize; the absence of the Montreal Protocol as computed by Chipperfield et al. (2015) has mostly exaggerated situations with already high UV values,

We have looked for the maximum UV effect both practical (by looking directly at the difference between scenarios) and theoretical (by looking at the equations driving the model). The theoretical analysis has led us to the conclusion that an event causing a large depletion of ozone over the equator (where ozone dependency is highest), or an event causing an extension of a certain low level of ozone through the low-mid latitudes (where the latitude dependency is highest) would result in the most dramatic increases in UV index. The locations of the maxima as found in our data set agree with the theoretical approach, thus confirming this conclusion.

7.5 Thresholds

We have extensively studied where values of UV irradiance have changed, and by how much they have changed between a scenario with and without the Montreal Protocol. Yet we have not touched upon how these changes affect humans. As stated before, the scientific relevance of studying UV light is largely related to the effect that it has on life on earth. Scientists in the field of medicine have made efforts to parametrize this effect. This is done in particular for cancer rates and vitamin D deficiency in humans.

7.5.1 Skin cancer incidence

In a paper by Hatfield et al. (2009), the relation between UV exposure and non-melanoma skin cancer is investigated using a statistical model. One of the results is that there are statistical relations between exceedance of threshold UVI values and cancer incidence rates.

Location	Latitude	Annual MSR trend	Annual WAV trend	Difference WAV-MSR trend	Maximum monthly trend	Month of maximum trend	All-time maximum difference
Tromso	+69.7	0.11	0.51	0.40	1.44	Jul	0.51
Helsinki	+60.2	0.27	0.83	0.56	2.37	Jul	0.665
Moscow	+55.8	0.44	1.11	0.67	2.69	Jul	0.786
De Bilt	+52.1	0.35	1.05	0.70	3.15	Jun	0.746
Istanbul	+41.0	0.45	1.33	0.88	3.12	Jun	0.773
New York	+40.7	0.49	1.38	0.89	3.06	Jun	0.751
Seoul	+37.6	0.22	1.16	0.94	2.57	May	0.753
Tamanrasset	+22.8	0.16	1.41	1.25	2.03	Mar	0.698
Paramaribo	+5.8	0.17	1.35	1.18	1.83	Apr	0.509
Mogadishu	+2.0	-0.05	1.10	1.15	1.49	Oct	0.443
Cairns	-16.9	0.35	1.70	1.35	2.84	Jan	0.698
Antananarivo	-18.9	0.54	1.95	1.41	2.79	Feb	0.778
Santiago	-33.5	0.40	1.67	1.27	2.94	Jan	1.128
Kaitaia	-35.1	0.54	1.71	1.17	3.40	Feb	1.057
Queenstown	-45.1	0.57	1.53	0.96	3.65	Jan	1.059
Ushuaia	-54.8	0.42	1.37	0.95	4.27	Nov	1.898

TABLE 7.1: Some statistics on the different scenarios at specific locations. Units of trends are $10^{-2} kJm^{-2}yr^{-1}$. Difference is in kJm^{-2}.

The most likely values for this threshold are UVI of 7 and 8, and 9 to a lesser degree. This research has been conducted using data from the region in the United States spanning latitudes 34° to 43° north and longitudes 90° to 78.75° west. Because of the spatial extent of this research, we assume spatial variation of cancer rates and UV index are accounted for, and that the same threshold values are valid for other parts of the world, given that the skin type is the same. We would like to apply these results to Europe, which extends further north and thus includes lower UVI values. Only summer days will be considered; the same days used by Hatfield et al. These are all days in the months May through September, 153 in total. The south of Europe (e.g. Spain, Italy, Greece) frequently has values exceeding the 7, 8 and 9 UVI thresholds; over 50-100 times per summer, varying per threshold. In the north of Europe (e.g. Scotland, Denmark) UVI values of 7 are exceeded a few times a year, but 8 and 9 only very rarely. The Netherlands in particular only very rarely reaches UVI values of 8; only twice or thrice in the decade before 2012.

The number of events when a certain threshold value is exceeded in 2012 is shown in figure 7.10. The year 2012 is chosen as this is the most recent year in the time series and is most representative of the current day situation (or the would-be current day situation, regarding the WAV scenario). The effect of the Montreal Protocol is also the greatest in the most recent year, so the differences between the scenarios are greatest.

Considering first the 7-threshold, the Netherlands is covered by at least some exceedance. When the UVI reaches 7, warnings are sent out in the Netherlands, so there have been ∼5 to 10 warnings in the summer of 2012. In the WAV scenario, the majority of the Netherlands lies just over the 50 counts contour, so there would have been 50 to 100 warnings; a tenfold increase. Countries further north also experience large differences. Scotland did not count any occurrences in the MSR scenario, meaning that the amount of UV light was not sufficient to affect cancer incidence in any significant way. The 0-to-1 contour, with zero occurrence towards the north, is replaced by the 19-to-20 contour. The change due to the absence of the Montreal Protocol is that Scotland would have had occurrences of UVI over 7 at least once everywhere, up to 20 times in the south. The change in Norway is also large. Where there were up to 5 occurrences in a specific area only - most likely related to high elevation - there are now up to and over 5 occurrences in the majority of (inhabited) Norway.

The change of the 8-threshold between scenarios is also large near the Netherlands. A UVI of 8 did not occur here in the MSR scenario in 2012, and only rarely occurred in other years. According to the paper by Hatfield et al., the posterior probability of the 8-threshold

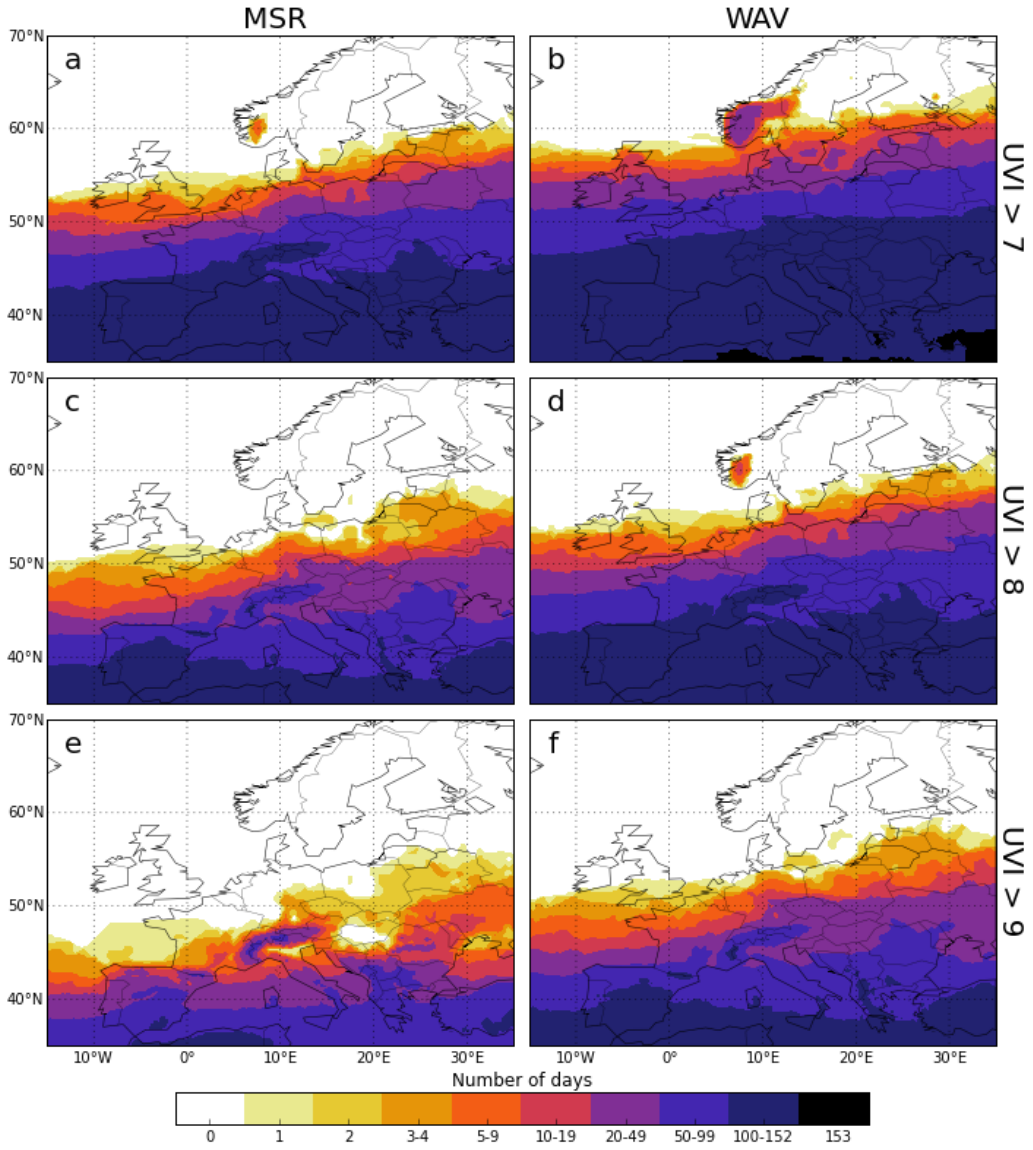

FIGURE 7.10: The number of times a threshold UVI is exceeded. From top to bottom are counts of threshold values 7, 8 and 9 respectively (a/b=7, c/d=8, e/f=9). The left column (a/c/e) shows of the MSR scenario, the right column (b/d/f) shows of the WAV scenario.

being related to cancer incidence is maximal (also equal to posterior probability of the 7-threshold) and cumulatively explains over 70% of cancer incidence. The Netherlands is mostly in the 'safe' zone with respect to the 8-threshold in the MSR scenario, but lies in the 5-9 occurrence range in the WAV scenario. According to the classification by the International Commission on Non-Ionizing Radiation Protection (ICNRP) and the World Health Organization (WHO), the Netherlands would occasionally have UVI values that are "Very High" instead of just "High" in the WAV scenario.

The occurrence of the 9-threshold has also shifted greatly. Hungary has increased from no exceedance to 20 to 50 counts. Other areas that never had any exceedance of a UVI of 9, like England and the Netherlands, now find one or two counts.

By comparing the UVI exceedance of 7 in the MSR scenario and of 8 in the WAV scenario (figures 7.10a and d), we see a very similar pattern. The patterns of figures 7.10c and f are equally similar. This implies that over Europe the Montreal Protocol has caused a reduction of UV indices by about one point regionally, and perhaps globally. More importantly, the 'danger zone' regarding exceedance of certain UVI thresholds has shifted in the WAV scenario and has increased incidence rate over areas mostly inhabited

by whites; the ethnic group with a high risk for skin cancer (Saraiya et al. 2004).

7.5.2 Vitamin D

The elevated UV levels from the WAV scenario also have beneficial health effects on humans. Vitamin D production in the skin is directly related to UV irradiance weighted by the vitamin D action spectrum. Vitamin D may have beneficial effects regarding cancer incidence and survival rates (Lim et al. 2006, Garland et al. 2006). So the WAV scenario may well be the more healthily beneficial scenario. We look for vitamin D thresholds as we did for cancer incidence threshold values in the previous subsection.

The vitamin D thresholds are derived from a study by Kelly et al. (2016). They studied plasma 25OHD in blood samples in relation to a cumulative weighted vitamin D UVD. The cumulative weight function decreases exponentially as a function of number of days before taking the blood sample and has a total weight of about 47 days. The thresholds for different risk categories are 10, 16 and 20ng mL^{-1} 25OHD for respectively deficient to high risk of deficiency, high to low risk of deficiency, and low risk of deficiency to sufficient. The 16 and 20ng mL^{-1} thresholds corresponds to covering the needs of 50% and $\geq$97.5% of the population (Ross et al. 2011). We use these two thresholds to relate to thresholds in UVD. Using the relation by Kelly et al. (2016) we find thresholds of cumulative UVD of 61 and 101kJ/m^2. Dividing this by the total weight of the cumulative weight function (47 days) we estimate daily UVD thresholds of 1.30 and 2.15kJ/m^2, respectively.

These thresholds are studied by counting the number of days below the threshold during the year 2012. Note that this is unlike the previous section, where the UVD *above* the threshold is counted: we count the amount of days in the 'danger zone'. Since vitamin D production is directly related to the UVD (unlike cancer to UVI, which is statistically related), we also count all-sky (including clouds) UVD as a more realistic representation. Counts of UVD below both thresholds are shown in figure 7.11 for clear and cloudy sky in the WAV and MSR scenario.

Consider first the threshold UVD<1.30kJ/m^2 for clear sky, focusing on the Netherlands. In the MSR scenario, over 55% of days has UVD below the threshold. Only 45% of days at most have UVD to keep half the population at a sufficient vitamin D level. The cloudy scenario is worse; with around 65% days of high deficiency risk. The increased UV levels of the WAV scenario cause a significantly lower count. Only about 50% of days is below the threshold, with slightly more days including clouds. The cloudy WAV scenario has a similar count to the clear MSR scenario (compare figures 7.11d and a) for the Netherlands and other parts of Europe (e.g. Germany, Romania).

Care has to be taken when interpreting the count of single days. In reality days contribute to vitamin D (25OHD) levels according to the cumulative weight function. The method adopted here (counting single days) should be interpreted as a count of days that do not contribute to sufficient vitamin D levels in the long run. People are not (at risk of being) vitamin D deficient each day the UVD is below the threshold. However, a count of e.g. 40% does imply people are (at risk of being) vitamin D deficient 40% of the time throughout the year[3].

Values of UVD below the 2.15kJ/m^2 threshold occur much more frequent. Regarding the clear sky MSR scenario, the Netherlands lies across the 70% count line. The Netherlands lie well in the >80% region in the (more realistic) cloudy scenario. The clear WAV scenario again appears to be the more healthy scenario. The cloudy WAV scenario shows most similarities to the clear MSR scenario (figures 7.11h and e), as it did for the UVD<1.30kJ/m^2 threshold, although not as striking as for the UVD<1.30kJ/m^2 threshold. This observation allows us to interpret the order of magnitude of the effect that the Montreal Protocol had (for Europe): Removing part of the ozone layer, which the Montreal Protocol prevented, has a similar effect on UV irradiance as removing all cloud cover throughout the year.

[3]If the only source of vitamin D is through UV exposure of the skin. Dietary intake of vitamin D reduces the risk of deficiency.

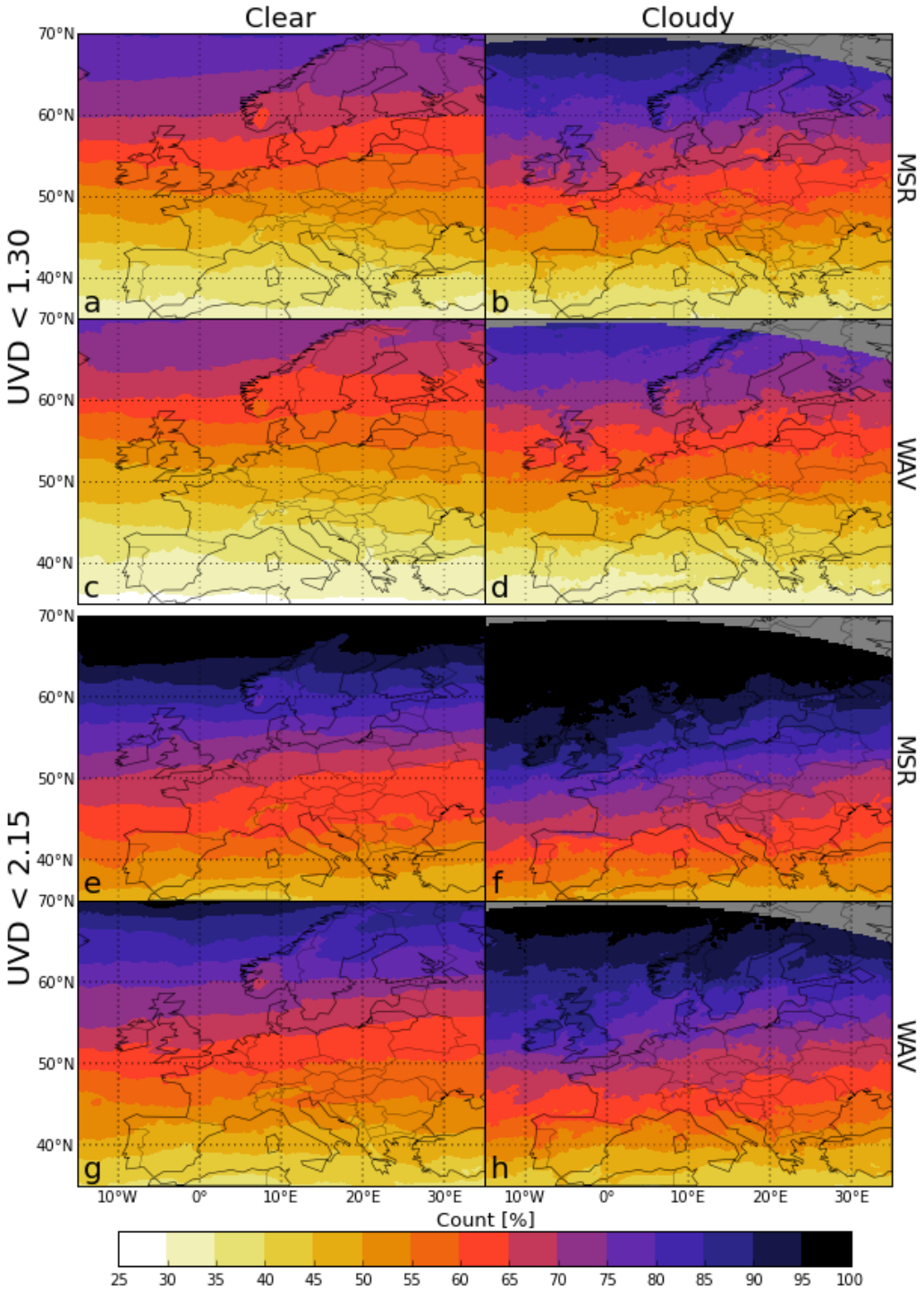

FIGURE 7.11: A count of days on which the UVD is below the threshold, including all days of 2012. The top 4 plots (a/b/c/d) count UVD<1.30kJ/m^2 and the bottom plots (e/f/g/h) count UVD<2.15kJ/m^2, as indicated on the left. All left plots (a/c/e/g) show counts of clear sky UVD and on the right (b/d/f/h) are counts of all-sky UVD, as indicated on top. Every other row of 2 plots shows UVD using either the MSR (a/b/e/f) or the WAV (c/d/g/h) ozone, as indicated on the right. Counts are shown in percentages of the 366 days in total.

	MSR	WAV	WAV - MSR	(WAV-MSR)/MSR
Erythemal	3.85	4.23	0.38	9.9%
Vitamin D	3.53	4.04	0.51	14.5%

TABLE 7.2: Comparison of the global annual average of 2012 clear sky UV doses. Units are kJ/m^2.

7.5.3 Total health effect

The action spectra for calculating the erythemal and vitamin D UVD are different (figure 2.1. A change in ozone will therefore have a different effect on either UVD type. In this section we have focused on the effect on human health. There are negative and positive effects, but it is not clear whether the overall effect of the Montreal Protocol has benefited humans. This question cannot be answered by this thesis alone. Expertise on medical effects is required to interpret the results presented here. However, there is one number that we *can* provide; the global increase in both types of clear sky UVD.

Daily data of the last year in the data set, 2012, is averaged temporally and spatially weighted by relative surface of each grid cell. The mean erythemal and vitamin D UVD in each scenario and their respective increases are shown in table 7.2.

7.6 Discussion

Throughout this chapter we have based various conclusions on data and results from different studies that we assumed applicable for our study. It has been mentioned in section 7.4.3 that high UV values in the WAV scenario are always paired with relatively high values in the MSR scenario. This is a result of the method by which the ozone for the absence of the Montreal Protocol has been modelled. A chemical transport model is used with varying boundary conditions regarding chemistry for each model. The meteorological boundary conditions are constant across both scenarios. However, changing the amount of ozone eventually leads to a change in meteorological conditions (e.g. a stronger and colder polar vortex) that promote further ozone depletion leading to further cooling, etc. The change in meteorology may further affect UV irradiance at the surface as cloud cover is expected to change as a result.

The lack of meteorological feedback leads to an underestimation of the ozone depletion. The method by which we utilize the data by Chipperfield et al. (2015) leads to further underestimation of ozone depletion in some situations. Because we are using monthly mean ozone data we smooth extremes of the computed ozone depletion from the data.

However, many of our findings are still valid in a more severe ozone-depleting scenario. The amount of UV irradiance is a combination of ozone values and solar zenith angle. Because ozone depletion occurred mostly where solar zenith angles are large, the resulting UVI or UVD is often low. If ozone depletion occurs where solar zenith are smaller, we expect larger UV changes in regions we identified as showing the largest change in UV: the mid to low latitudes. Our γ-parameter will prove useful to determine what gradients in ozone distribution cause extraordinary UV values, based on the location of the gradient and time of year.

We further assumed the results of Hatfield et al. (2009) to be applicable to Europe. This may be a wrong assumption as the situation that has been studied is quite different from Europe regarding UVI count. The 7-threshold, for example, is exceeded at least 100 times per summer everywhere in the domain, even in the MSR scenario. In Europe we are explicitly looking at regions where thresholds are exceeded either zero times or once and more. The research by Hatfield et al. (2009) did not treat value of exceedance (the threshold value) and number of exceedance (the count) separately. The 7-threshold, for example, held a statistical relation to cancer incidence, given the actual exceedance count of the 7-threshold. There may have been an additional intrinsic threshold in count; perhaps a count of 30 is important to affect cancer incidence at all. Such a count threshold is always exceeded in the domain of Hatfield et al., but this is not what we chose to study in Europe.

Chapter 8

Conclusions

8.1 Improvements

The UV model has been improved by updating the input data and the algorithm. The calculation regarding the ground elevation is changed in two ways that are both considered improvements. Changing the resolution from 0.5° to 0.25° results in more specific information on UV irradiance for every location. Changing from the GTOPO30 to the GMTED2010 map is an improvement as the GMTED2010 map is a newer version.

Changing the albedo map is also considered an improvement. Both TOMS/GOME and GOME-2 maps have advantages over the other, but the GOME-2 map is considered better mainly for its higher spectral resolution. Time interpolation between monthly climatologies is considered an improvement by statistical arguments: a gradually changing albedo is more likely to properly represent each day's albedo on average than allowing jumps in albedo after the last day of each month.

The UV error estimate, provided to inform the user of the reliability of the data, has also been improved. Previously only the ozone error was available for computation of the total error on the UV product. The updated surface albedo and ground elevation data are available with error estimates, which have been added to the total UV error.

The computation of the cloud attenuation factor has been revised. We consider this an improvement since the newly available data includes more detailed cloud properties than the previously available data. Validation is required to show that the revision is indeed an improvement, although comparison with the previous method is already promising. Regardless of the change in method, the region for which cloud information is available has increased greatly, including Africa and surroundings in addition to Europe.

8.2 World-avoided scenario

If the Montreal Protocol had not been adopted, total column ozone values would have decreased and consequently UV irradiance at the surface would have increased. The largest decreases in ozone usually lead to the largest increases in UV. At the poles this is not necessarily true due to the large solar zenith angle. Specifically the 2011 would-be ozone hole on the northern hemisphere was paired with very low UVD values. The largest absolute change in UV was observed at mid to low latitudes, while the largest relative change occurred at mid to high latitudes, which we confirmed theoretically. We found that the increased UV values could be interpreted as a poleward shift of values (about 9 degrees in summer) or an extension of the summer season (up to 2 months). Additionally, we found a method to classify ozone distributions by what type of UV behavior they result in. With this method we explained the difference between a particular Antarctic ozone hole distribution and the distribution during the would-be Arctic ozone hole.

The effects on human health is quantified in terms of exceedance of thresholds of UVI and UVD. The UVI threshold of 7, relevant for skin cancer and the level at which a UV warning is sent out in the Netherlands, is exceeded almost ten times more in the world-avoided scenario than in the real world in 2012. An estimate of the order of magnitude of the effect of the Montreal Protocol, regarding vitamin D deficiency, is made: Removing part of the ozone layer, which the Montreal Protocol prevented, has a similar effect on UV irradiance as removing all cloud cover throughout the year. Nevertheless, whether the

effect of the Montreal Protocol has benefited human beings depends on whether the skin cancer benefits outweigh the vitamin D detriment.

Chapter 9

Outlook

The improvements described in this thesis make the model a state-of-the-art empirical UV model. Some aspects that have been changed (i.e. ground elevation and surface albedo) cannot be improved on further until new data or developments become available. The calculation of the cloud attenuation factor however, can still be improved. The assumption that the CAF can be represented by the SDS-ratio requires confirmation, which can be done by validating the resulting UVD with groundbased measurements. Furthermore, the single-band SDS ratios are available over a limited time only, but may soon become available for the full MSG data period. This allows the CAF to be directly calculated from the single-band SDS ratios instead of using the broad-band SDS ratio with a fit function.

Further improving the model can be done by including variation in quantities that is not accounted for in the model currently. The sky albedo used in the surface albedo parameterization and aerosol optical depth are assumed to be globally constant: 0.25 and 0.346, respectively. With the new method for cloud attenuation, a varying sky albedo is introduced as a result from the SDS ratio. The sky albedo can also be computed for the UV model using different output from the SICCS model, and is thus available to great detail which is not currently utilized. The effect of aerosols on the UVI has been studied (Badosa & van Weele 2002), and near-real time aerosol data is available to the KNMI. Implementing aerosol information may improve the accuracy of the model by about 5% (Allaart et al. 2004).

Regarding application of the model, any ozone scenario is well fit to be applied to our model. Ozone concentrations (in the stratosphere) do not directly relate to any health effects, whereas the UVI and UVD do. The world-avoided scenario studied in this thesis, a world in which the Montreal Protocol was not adopted, can be studied further regarding health effects. Various types of analysis are done to study the relation between the input ozone fields and the output UV product. This has served to locate the regions where the impact of the ozone change is largest. Studying the health effects in these regions is the main interest, as this is the primary reason for translating ozone to surface UV irradiance. Interpretation of the results regarding skin cancer incidence and vitamin D can still be expanded, although this is largely dependent on how scientists in the field of medicine quantify the effect of UV irradiance on humans. The study by Juzeniene et al. (2014), where a direct relation between cancer incidence rates and UVD is found using sigmoidal curves, may be a promising addition.

Bibliography

van der A, R.J., Allaart, M.A.F., Eskes, H.J. (2015) Extended and refined multi sensor reanalysis of total ozone for the period 1970–2012. *Atmos. Meas. Tech.* **8**: 3021-3035

Acosta, L.R., Evans, W.F.J. (2000) Design of the Mexico City UV monitoring network: UV-B measurements at ground level in the urban environment. *J. Geophys. Res.* **105**: D4, 5017-5026

Allaart, M., van Weele, M., Fortuin, P., Kelder, H. (2004) An empirical model to predict the UV-index based on solar zenith angles and total ozone. *Meteorol. Appl.* **11**: 59-65

ASTM Standard G173 - 03 (Reapproved 2012), Standard Tables for Reference Solar Spectral Irradiances: Direct Normal and Hemispherical on 37°Tilted Surface; ASTM International: West Conshohocken, PA, 2012. doi:10.1520/G0173-03R12

Badosa J. (2002) Mesures d'Irradiancia eritematica a Catalunya vs modelitzacions per cels serens a partir de la columna d'ozo d'EP/TOMS *Minor thesis*

Badosa J., van Weele, M. (2002) Effects of aerosols on uv-index. *KNMI scientific report; WR-2002-07*, ISBN: 90-369-2222-4

Basart, S., Benedictow, A., Blechschmidt, A.-M., Chabrillat, S., Christophe, Y., Clark, H., Cuevas, E., Flentje, H., Hansen, K.M., Im, U., Kapsomenakis, J., Langerock, B., Richter, A., Schulz M., Sudarchikova, N., Thouret, V., Wagner, A., Zerefos, C. (2016) Validation report of the CAMS near-real time global atmospheric composition service. *CAMS84_2015SC1_D.84.1.2-2016Q1_201602*, February 29, 2016

Bell, M.L., Davis, D.L., Fletcher, T. (2004) A retrospective assessment of mortality from the London Smog Episode of 1952: The role of influenza and pollution. *Env. Health Persp.* **112**(1): 6-8

Bernhard, G., Seckmeyer, G. (1997) Measurements of spectral solar UV irradiance in tropical Australia. *J. Geophys. Res.* **102**: 8719-8730

Boersma, K.F., Eskes, H.J., Brinksma, E.J. (2004) Error analysis for tropospheric NO_2 retrieval from space. *J. Geophys. Res.* **109**: D04311.

Bouillon, R., Eisman, J., Garabedian, M., Holick, M., Kleinschmidt, J., Suda, T., Terentskaya, I., Webb, A. (2006) Action spectrum for the production of previtamin D_3 in human skin. *CIE technical report* ISBN: 3-901-906-50-9

Burrows, J.P., Holzle, E., Goede, A.P.H., Visser, H., Fricke, W. (1995) SCIAMACHY - Scanning imaging absorption spectrometer for atmospheric chartography. *Acta Astronaut* **35**: 445-451

Burrows, W.R., Vallée, M., Wardle, D.I., Kerr, J.B., Wilson, L.J., Tarasick, D.W. (1994) The Canadian operational procedure for forecasting total ozone and UV radiation. *Meteorol. Appl.* **1**(3): 247-265

Caldwell, Martyn M. (1971) Solar UV irradiation and the growth and development of

higher plants. *Photophysiology* **6**: 131-177

Chipperfield, M.P., Dhomse, S.S., Feng, W., McKenzie, R.L., Velders, G.J.M., Pyle, J.A. (2015) Quantifying the ozone and ultraviolet benefits already achieved by the Montreal Protocol. *Nat. Comm.* **6**: 7233

Dahlback, A., Norsang, G., Stamnes, J.J., Gjessing, Y. (2007) UV measurements in the 3000-5000 m altitude region in Tibet. *J Geophys. Res.* **112**: D09308

Danielson, J.J., Gesch, D.B. (2011) Global multi-resolution terrain elevation data 2010 (GMTED2010). *U.S. Geol. Surv. Open File Rep.*, 2011-1073: 25pp

Derrien, M., Le Gléau, H., Fernandez, P. (2013) Algorithm Theoretical Basis Document for "Cloud Products" (CMa-PGE01 v3.2, CT-PGE02 v2.2 & CTTH-PGE03 v2.2) *SAF/NWC/CDOP2/MFL/SCI/ATBD/01*, issue 3.2.1, July 15, 2013

Eskes, H.J., van Velthoven, P.F.J., Valks, P.J.M., Kelder, H.M. (2003) Assimilation of GOME total-ozone satellite observations in a three-dimensional tracer-transport model. *Q. J. R. Meteorol. Soc.* **129**: 1663-1681

Farman, J.C., Gardiner, B.G., Shanklin, J.D. (1985) Large losses of total ozone in Antarctica reveal seasonal ClO_x/NO_x interaction *Nature* **315**: 207-210

Fernández, P. (2012) SAF NWC/MSG output products format definition. *SAF/NWC/CDOP/INM/SW/ICD/3*, Issue 6, February 15, 2012.

Foyo-Moreno, I., Alados, I., Alados-Arboledas, L. (2007) Adaptation of an empirical model for erythemal ultraviolet irradiance. *Ann. Geophys.* **25**: 1499-1508

Garland, C.F., Mohr, S.B., Gorham, E.D., Grant, W.B., Garland, F.C. (2006) Role of Ultraviolet B Irradiance and Vitamin D in Prevention of Ovarian Cancer. *Am. J. Prev. Med.* **31**: 512-514

van Geffen, J., van der A, R., van Weele, M., Allaart, M., Eskes, H. (2005) Surface UV radiation monitoring based on GOME and SCIAMACHY. *Proceedings of the ENVISAT & ERS Symposium, 6–10 September 2004, ESA publication SP-572*, Salzburg, Austria

Gesch, D.B., Verdin, K.L., Greenlee, S.K. (1999) New land surface digital elevation model covers the Earth. *Earth & Space Science News* **80** (6): 69-70

Giese, A.C. (2013) Photophysiology: Current topics in Photobiology and Photochemistry. *Elsevier Science* ISBN: 9781483262215

Greuell, W., Meirink, J.F., Wang, P. (2013) Retrieval and validation of global, direct, and diffuse irradiance derived from SEVIRI satellite observations. *J. Geophys. Res: Atm.* **118**: 2340-2361

Gueymard, C.A., Myers, D., Emery, K. (2002) Proposed reference irradiance spectra for solar energy systems testing. *Solar Energy* **73**: 443-467

Häder, D.-P., Kumar, H.D., Smith, R.C., Worrest, R.C. (2007) Effects of solar UV radiation on aquatic ecosystems and interactions with climate change. *Photochem. Photobiol. Sci.* **6**: 267-285

Hatfield, L.A., Hoffbeck, R.W., Alexander, B.H., Carlin, B.P. (2009) Spatiotemporal and spatial threshold models for relating UV exposures and skin cancer in the central United States. *Comput. Stat. Data Anal.* **53**: 3001-3015

Herman, J.R., Celarier, E.A. (1997) Earth surface reflectivity climatology at 340-380 nm from TOMS data. *J. Geophys. Res.* **102**(D23): 28003-28011

Holick, M.F. (2007) Vitamin D deficiency. *N Engl J Med.* **357**: 266-281

Holick, M.F., Binkley, N.C., Bischoff-Ferrari, H.A., Gordon, C.M., Hanley, D.A., Heaney, R.P., Murad, M.H., Weaver, C.M. (2011) Evaluation, treatment, and prevention of vitamin D deficiency: an endocrine society clinical practice guideline. *J. Clin. Endocrinol. Metab.* **96**(7): 1911-1930

Holton, J.R., Curry, J.A., Pyle, J.A (2002) Encyclopedia of Atmospheric Sciences. *Elsevier Science* ISBN: 978-0-12-227090-1

Juzeniene, A., Grigalavicius, M., Baturaite, Z., Moan, J., (2014) Minimal and maximal incidence rates of skin cancer in Caucasians estimated by use of sigmoidal UV dose-incidence curves. *Int. J. Hyg. Env. Health* **217**: 839-844

Kaurola, J., Lindfors, A., Lakkala, K., Hansen, G., Josefsson, W., Vuilleumier, L., Feister, U., Slaper, H. (2010) On the usability of the ERA-40 reanalysis in the estimation of past surface UV radiation over Europe. *J. Geophys. Res.* **115**: D24107

Kelly, D., Theodoratou, E., Farrington, S.M., Fraser, R., Campbell, H., Dunlop, M.G., Zgaga, L. (2016) The contributions of adjusted ambient ultraviolet B radiation at place of residence and other determinants to serum 25-hydroxyvitamin D concentrations. *Brit. J. Derm.* **174**: 1068-1078

Koelemeijer, R.B.A., de Haan, J.F., Stammes, P. (2003) A database of spectral surface reflectivity in the range 335-772 nm derived from 5.5 years of GOME observations. *J. Geophys. Res.* **108**(D2): 4070

Koepke, P., Bais, A., Balis, D., Buchwitz, M., De Backer, H., de Cabo, X., Eckert, P., Eriksen, P., Gillotay, D., Heikkilä, A., Koskela, T., Lapeta, B., Litynska, Z., Lorente, J., Mayer, B., Renaud, A., Ruggaber., A, Schauberger, G., Seckmeyer, G., Seifert, P., Schmalwieser, A., Schwander, H., Vanicek, K., Weber, M. (1998) Comparison of models used for UV index calculations. *Photochem. Photobiol.* **67**(6): 657-662

Lim, H.S., Roychoudhuri, R., Peto, J., Schwartz, G., Baade, P., Moller, H. (2006) Cancer survival is dependent on season of diagnosis and sunlight exposure. *Int. J. Cancer* **119**: 1530-1536

Madronich, S. (2007) Analytic formula for the clear-sky UV index. *Photochem. Photobiol.* **83**: 1537-1538

McKinlay, A., Diffey, B.L. (1987) A reference action spectrum for ultra-violet induced erythema in human skin. In: W.F. Passchier & B.F.M. Bosnajakovic (eds.), *Human Exposure to Ultra-violet Radiation: Risks and Regulations*, Amsterdam: Elsevier, 83-87

Molina, M.J., Rowland, F.S. (1974) Stratospheric sink for chlorofluoromethanes: chlorine atom-catalysed destruction of ozone. *Nature* **249**: 810-812

den Outer, P.N., Slaper, H., Kaurola, J., Lindfors, A., Kazantzidis, A., Bais, A.F., Feister, U., Junk, J., Janouch, M., Josefsson, W. (2010) Reconstruction of erythemal ultraviolet radiation levels in Europe for the past 4 decades. *J. Geophys. Res.* **115**: D10102

Ross, A.C., Manson, J.E., Abrams, S.A., Aloia, J.F., Brannon, P.M., Clinton, S.K., Durazo-Arvizu, R.A., Gallagher, J.C., Gallo, R.L., Jones, G., Kovacs, C.S., Mayne, S.T., Rosen, C.J., Shapses, S.A. (2011) The 2011 report on dietary reference intake for calcium and vitamin D from the institute of medicine: What clinicians need to know. *J. Clin.*

Endocrinol. Metab. **96**(1): 53-58

Saraiya, M., Glanz, K., Briss, P.A., Nichols, P., White, C., Das, D., Jay Smith, S., Tannor, B., Hutchinson, A.B., Wilson, K.M., Gandhi, N., Lee, N.C., Rimer, B., Coates, R.C., Kerner, J.F., Hiatt, R.A., Buffler, P., Rochester, P. (2004) Interventions to prevent skin cancer by reducing exposure to ultraviolet radiation. *Am. J. Prev. Med.* **27**(5): 422-466

Stubenrauch, C.J., Rossow, W.B., Kinne, S., Ackerman, S., Cesana, G., Chepfer, H., Di Girolamo, L., Getzewich, B., Guignard, A., Heidinger, A., Maddux, B.C., Menzel, W.P., Minnis, P., Pearl, C., Platnick, S., Poulsen, C., Riedi, J., Sun-Mack, S., Walther, A., Winker, D., Zeng, S., Zhao, G. (2013) Assessment of Global Cloud Datasets from Satellites: Project and Database Initiated by the GEWEX Radiation Panel. *B. Am. Meteorol. Soc.* **94**(7): 1031-1049

Tilstra, L.G., Tuinder, O.N.E., Stammes, P. (2015) GOME-2 surface LER product - Algorithm Theoretical Basis Document. *KNMI Report O3MSAF/KNMI/ATBD/003*, Issue 1.7, October 26, 2015.

Vanicek, K., Frei, T., Litynska, Z., Schmalwieser, A. (2000) UV-Index for the public. A guide for publication and interpretation of solar UV Index forecasts for the public prepared by the Working Group 4 of the COST-713 Action "UVB Forecasting". *COST-713 Action, European Commission, Luxembourg*, ISBN: 92-828-8142-3

van Weele, M., van der A, R.J., Roebeling, R. (2005) Space-based surface UV monitoring for Europe using SCIAMACHY and MSG. *Proceedings of the 12th SPIE International Symposium on Remote Sensing*, 19-22 September 2005, Bruges, Belgium, 8pp

World Health Organization (2002) Global solar UV index: A practical guide. ISBN: 92-4-159007-6

Zuk-Golaszewska, K., Upadhyaya, M.K., Golaszewski, J. (2003) The effect of UV-B radiation on plant growth and development. *Plant Soil Environ.* **49**(3): 135-140

Appendices

Appendix A

Monthly mean UVD values per year in various cities around the world.

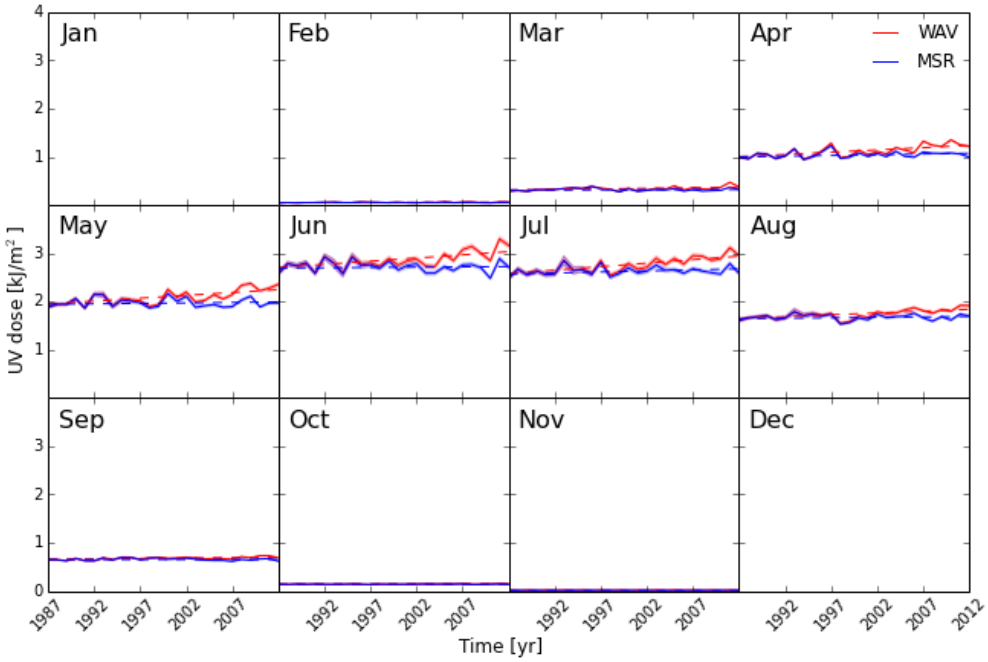

Monthly mean UV dose values in **Tromsø**, Norway.

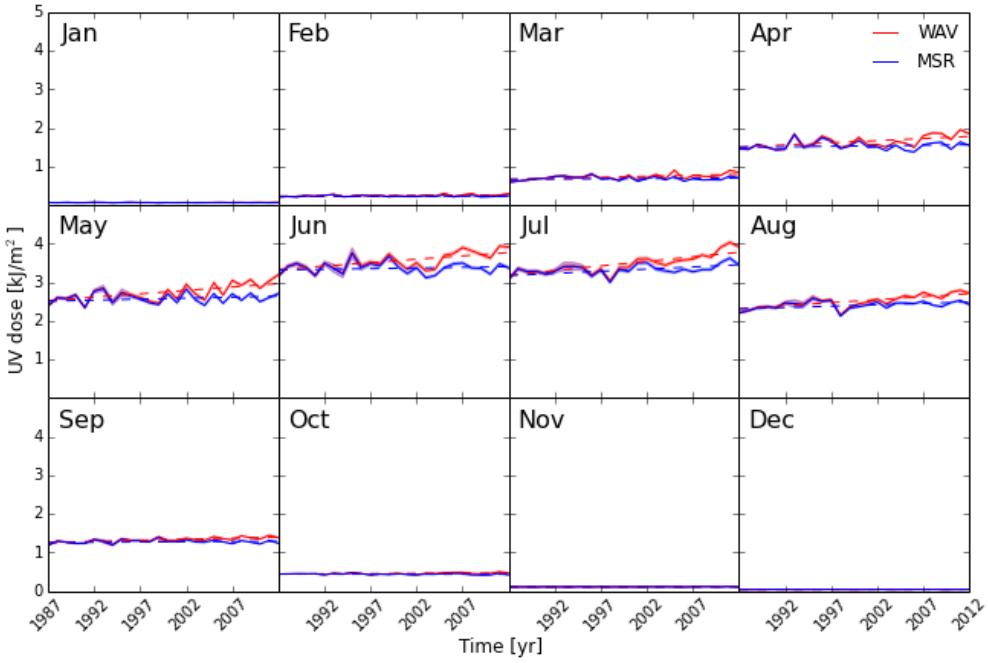

Monthly mean UV dose values in **Helsinki**, Finland.

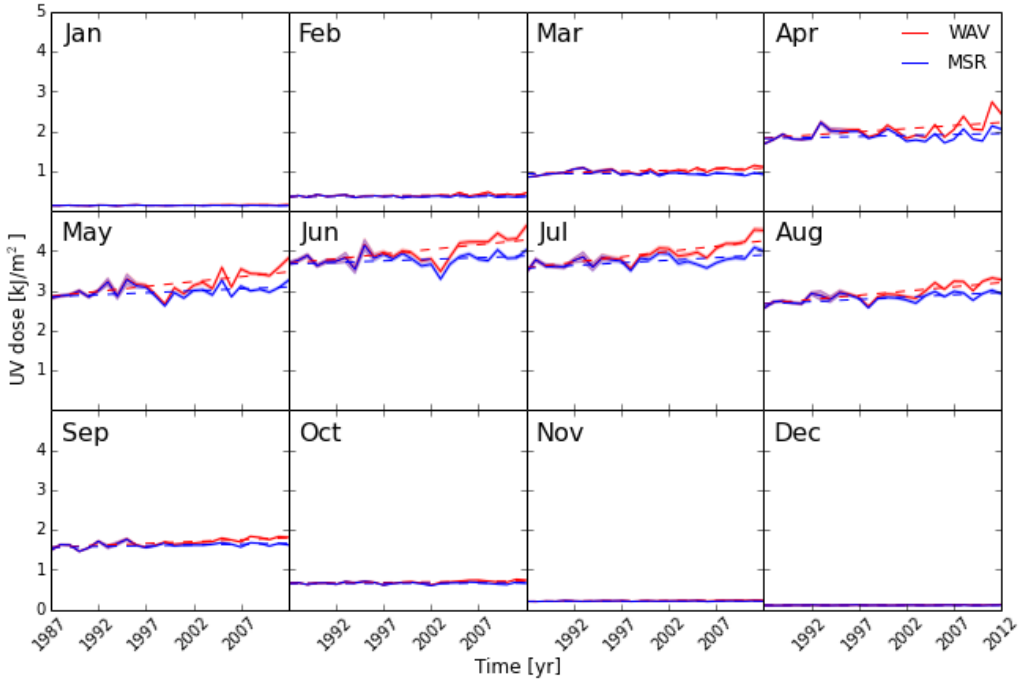

Monthly mean UV dose values in **Moscow**, Russia.

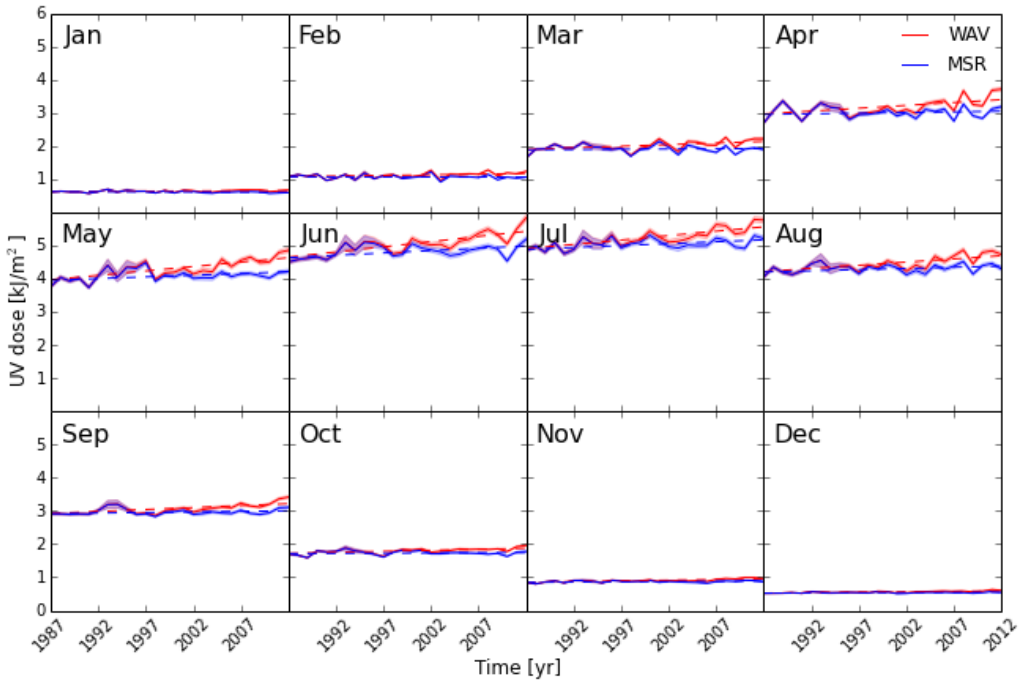

Monthly mean UV dose values in **Istanbul**, Turkey.

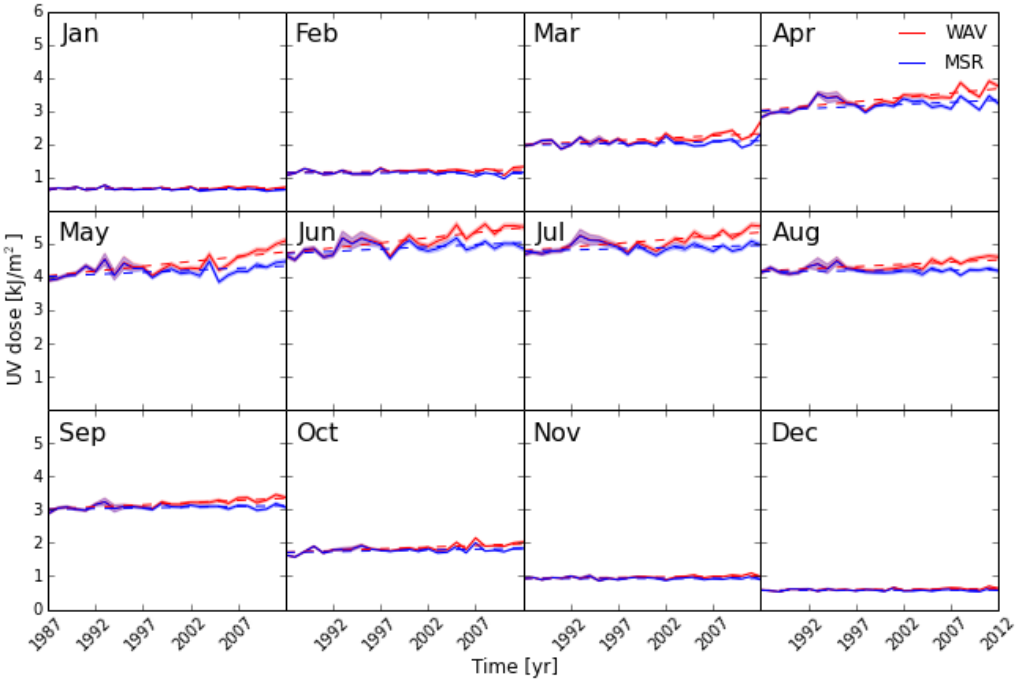

Monthly mean UV dose values in **New York**, United States.

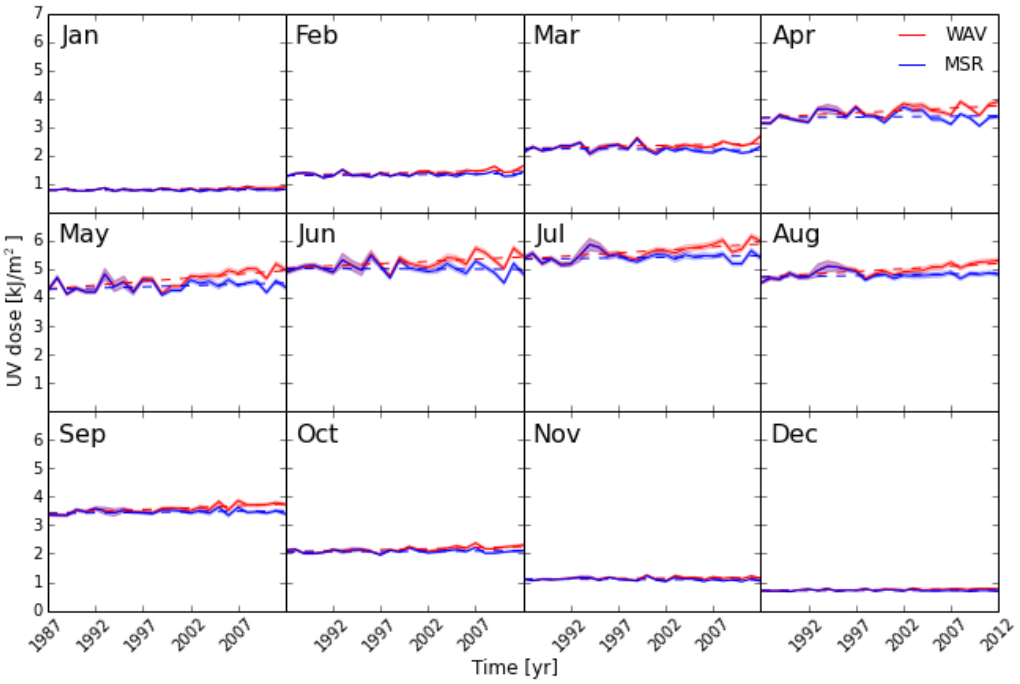

Monthly mean UV dose values in **Seoul**, South Korea.

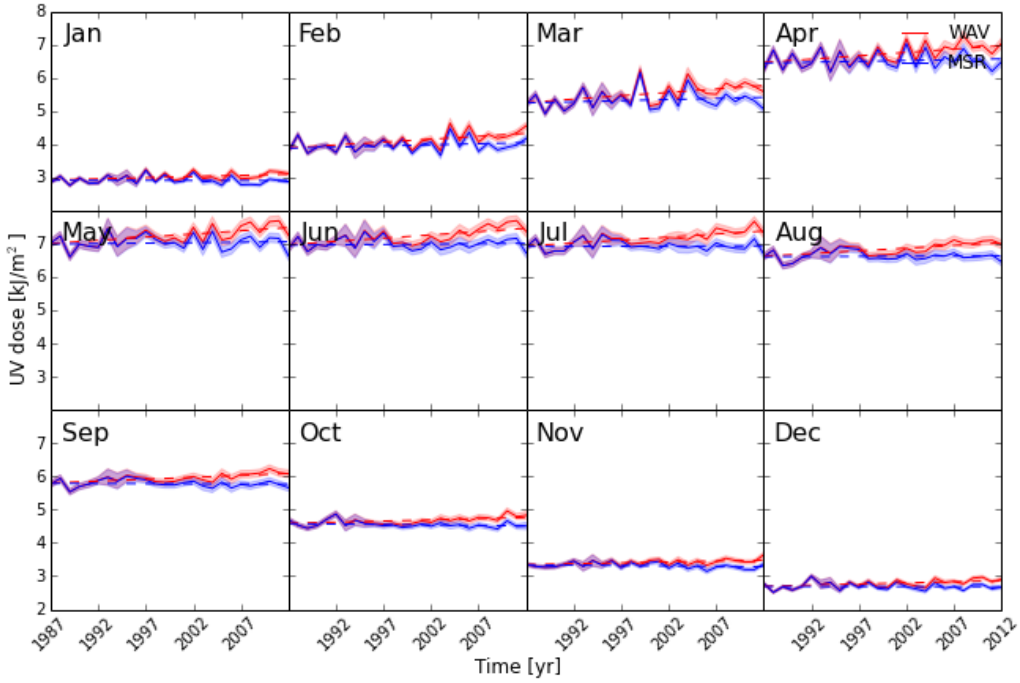

Monthly mean UV dose values in **Tamanrasset**, Algeria.

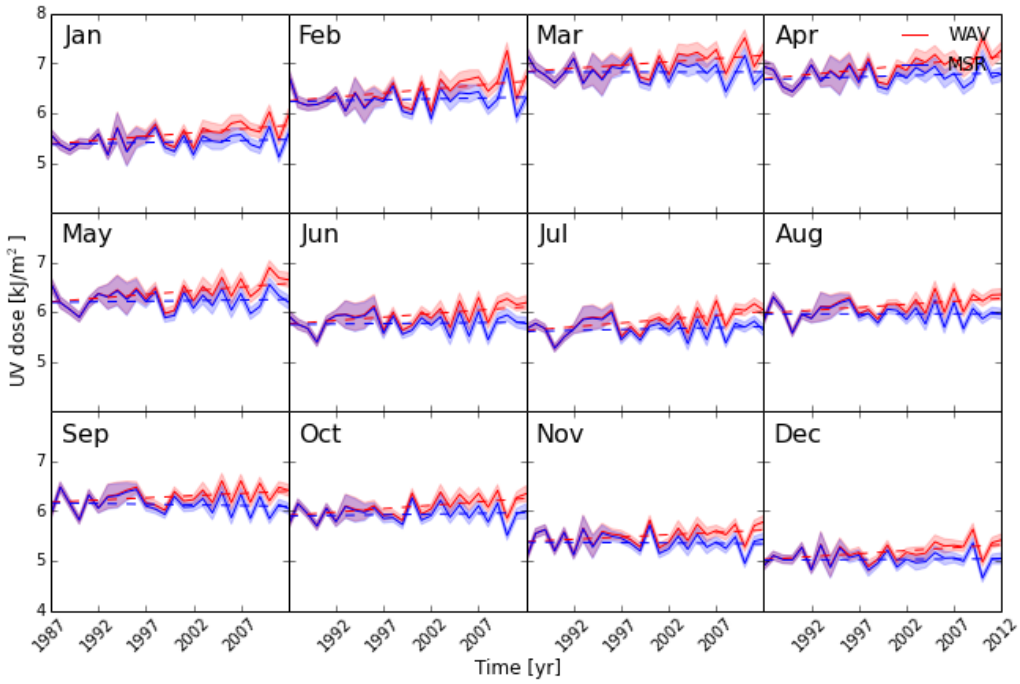

Monthly mean UV dose values in **Paramaribo**, Surinam.

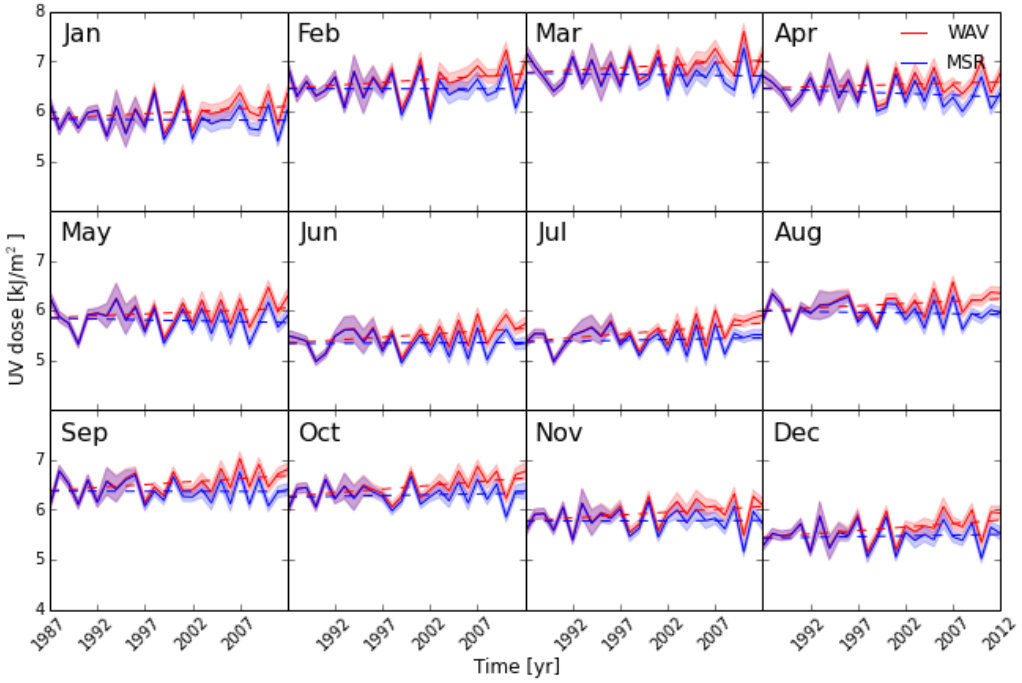

Monthly mean UVD values in **Mogadishu**, Somalia.

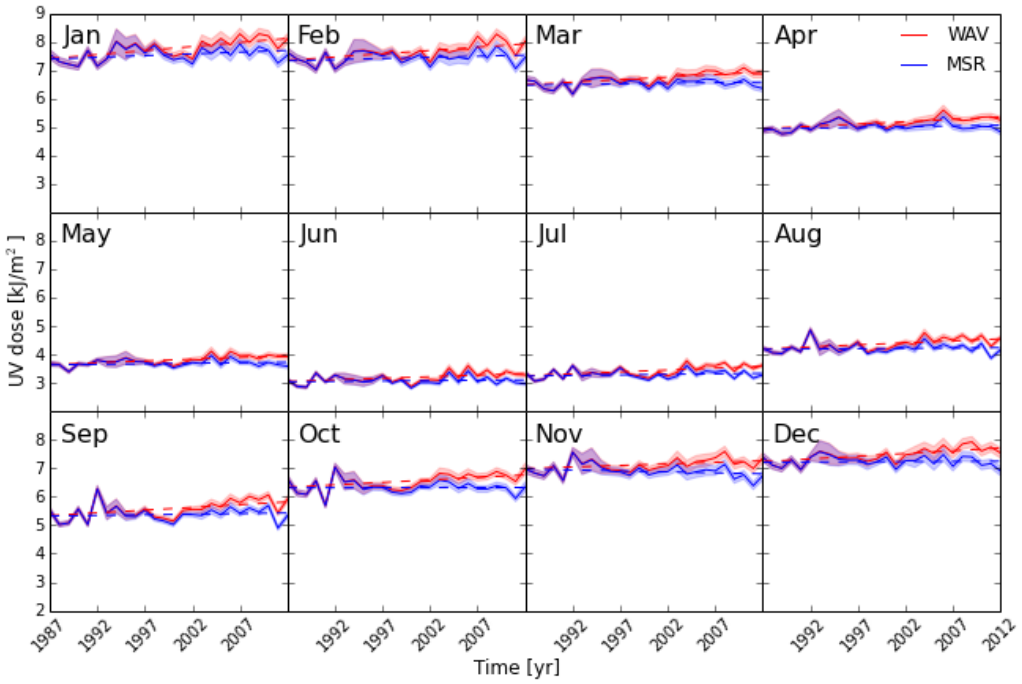

Monthly mean UVD values in **Cairns**, Australia.

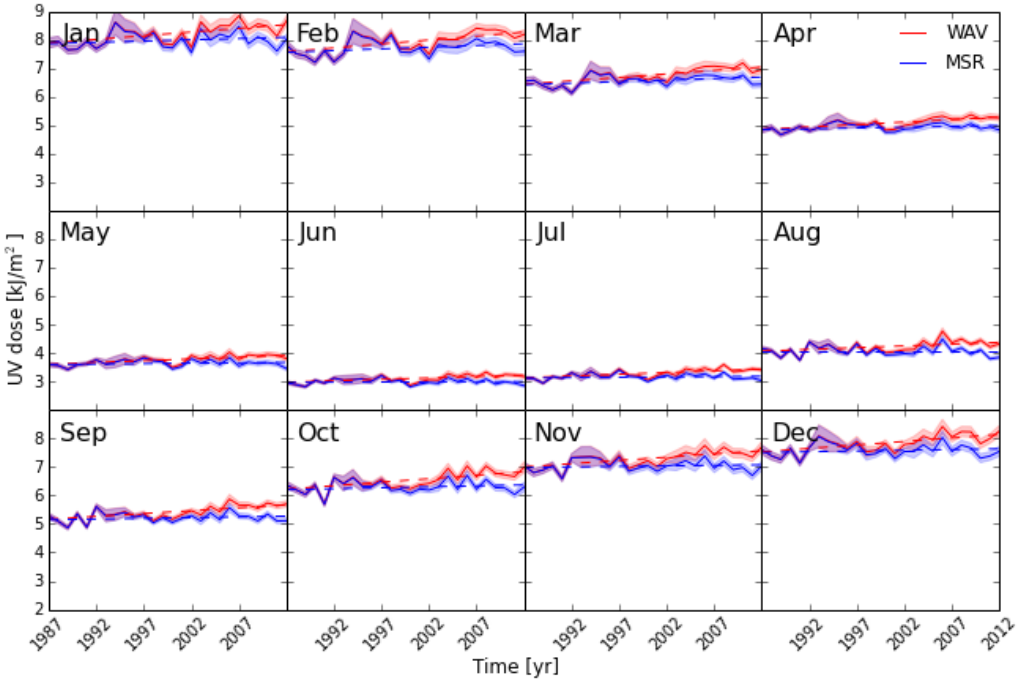

Monthly mean UVD values in **Antananarivo**, Madagascar.

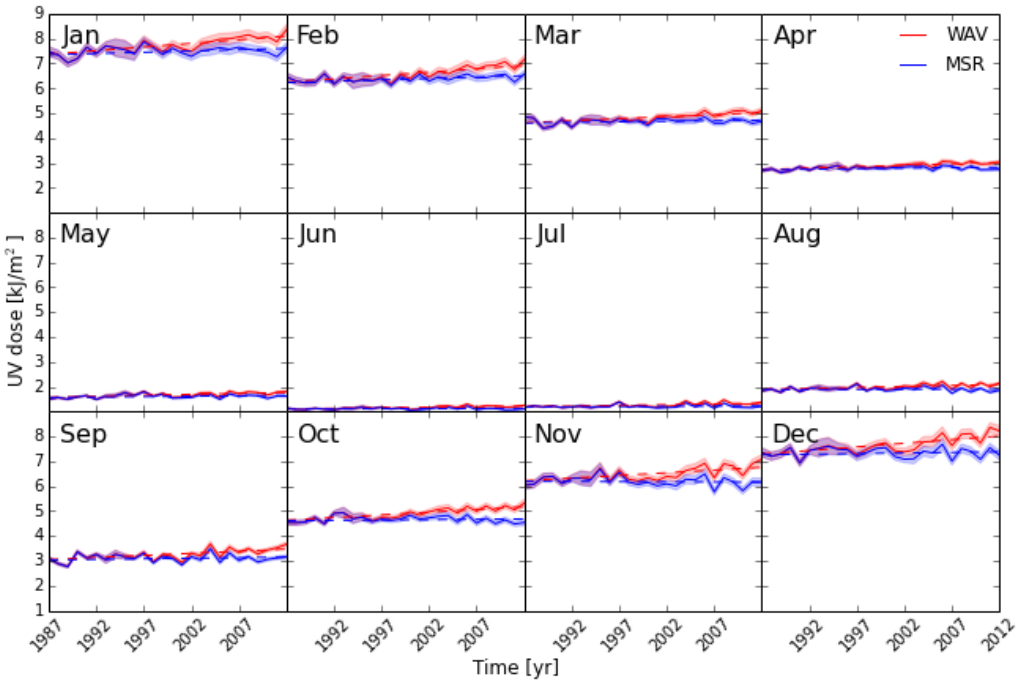

Monthly mean UVD values in **Santiago**, Chile.

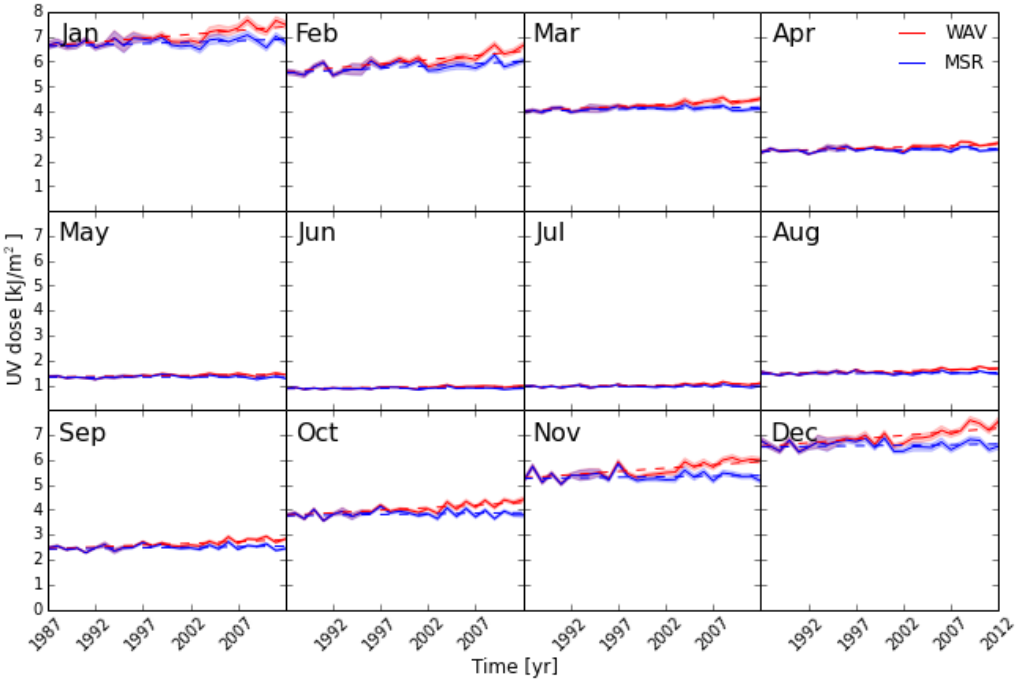

Monthly mean UVD values in **Kaitaia**, New Zealand.

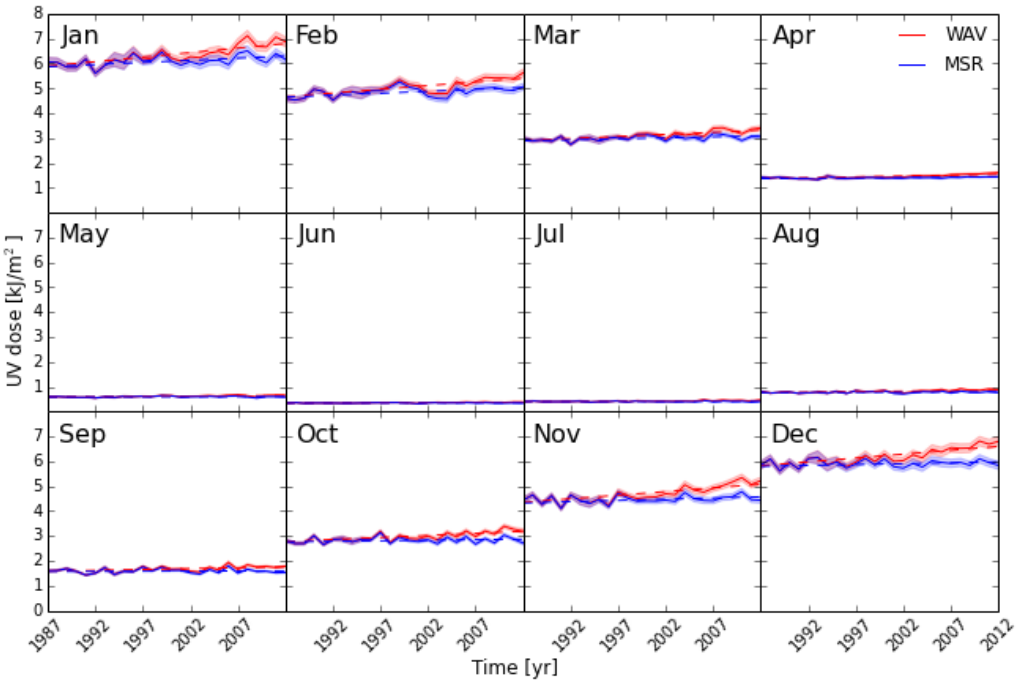

Monthly mean UVD values in **Queenstown**, New Zealand.

Appendix B

Difference in UVD between the WAV and MSR scenarios.

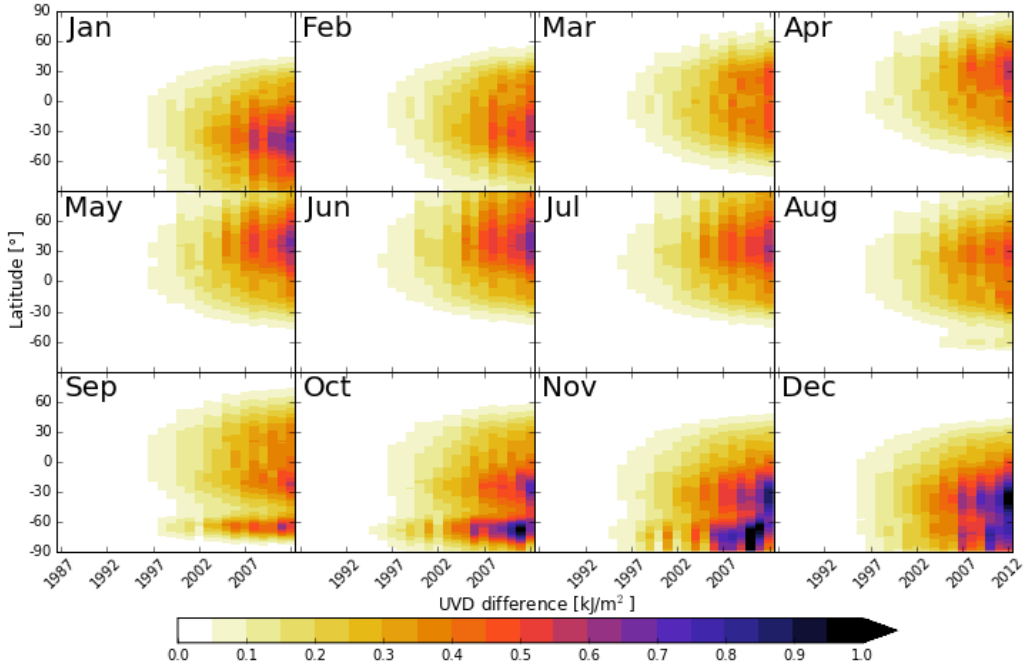

Zonal monthly mean UVD difference between WAV and MSR scenarios.

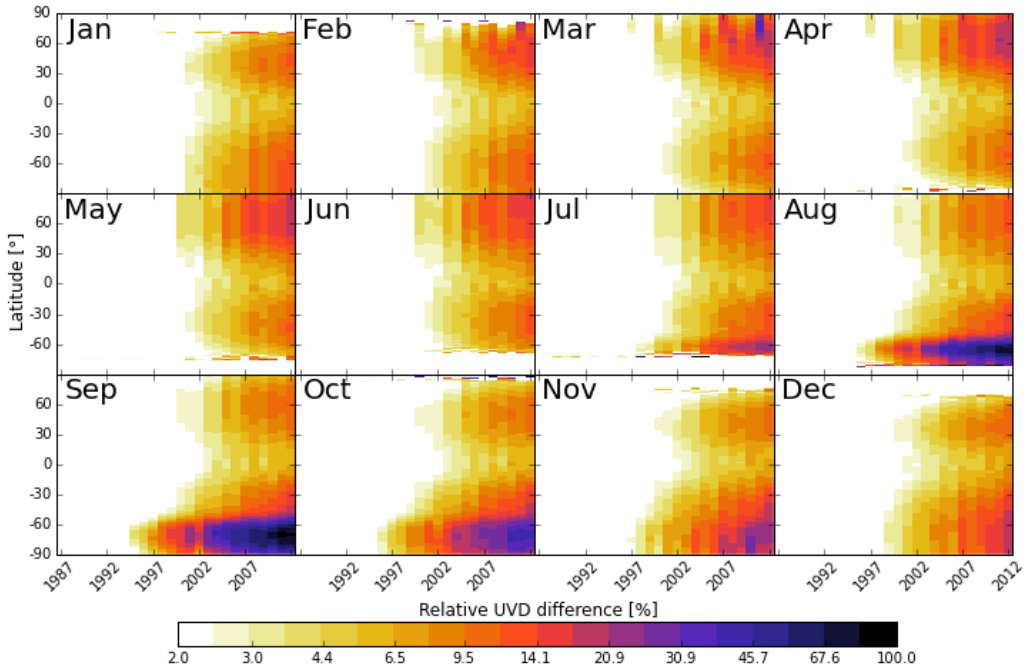

Zonal monthly mean relative UVD difference between WAV and MSR scenarios.